



저작자표시-동일조건변경허락 2.0 대한민국

이용자는 아래의 조건을 따르는 경우에 한하여 자유롭게

- 이 저작물을 복제, 배포, 전송, 전시, 공연 및 방송할 수 있습니다.
- 이차적 저작물을 작성할 수 있습니다.
- 이 저작물을 영리 목적으로 이용할 수 있습니다.

다음과 같은 조건을 따라야 합니다:



저작자표시. 귀하는 원저작자를 표시하여야 합니다.



동일조건변경허락. 귀하가 이 저작물을 개작, 변형 또는 가공했을 경우에는, 이 저작물과 동일한 이용허락조건하에서만 배포할 수 있습니다.

- 귀하는, 이 저작물의 재이용이나 배포의 경우, 이 저작물에 적용된 이용허락조건을 명확하게 나타내어야 합니다.
- 저작권자로부터 별도의 허가를 받으면 이러한 조건들은 적용되지 않습니다.

저작권법에 따른 이용자의 권리는 위의 내용에 의하여 영향을 받지 않습니다.

이것은 [이용허락규약\(Legal Code\)](#)을 이해하기 쉽게 요약한 것입니다.

[Disclaimer](#)

Thesis for the Degree of Master of Engineering

A Study on T-phase Phosphor in Binary Ba_2SiO_4 - Ca_2SiO_4 Systems for
White-Light-Emitting Diode



by

Kwang Won Park

Department of Image System Science and Engineering

The Graduate School

Pukyong National University

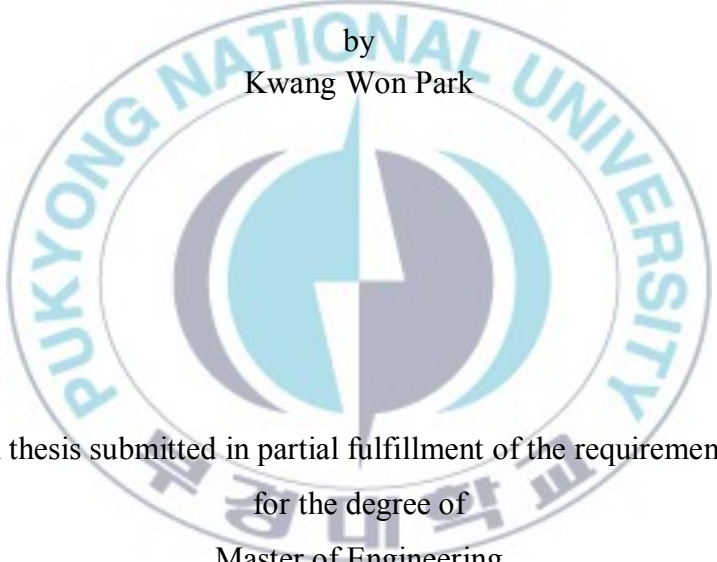
February 2010

A Study on T-phase Phosphor in Binary Ba_2SiO_4 - Ca_2SiO_4 Systems for
White-Light-Emitting Diode

(Ba_2SiO_4 - Ca_2SiO_4 이성분계내 백색 발광 소자용 T-phase 형광체 특성 연구)

Advisor: Prof. Jong Su Kim

by
Kwang Won Park

The logo of Pukyong National University is a circular emblem. It features a stylized 'P' and 'U' intertwined in the center, with the university's name 'PUKYONG NATIONAL UNIVERSITY' written in a circle around the emblem. Below the emblem, the Korean name '북경대학교' is also visible.

A thesis submitted in partial fulfillment of the requirements
for the degree of
Master of Engineering

in Department of Image System Science and Engineering, The Graduate School,
Pukyong National University

February 2010

A Study on T-phase Phosphor in Binary Ba_2SiO_4 - Ca_2SiO_4 Systems for
White-Light-Emitting Diode

A thesis

by

Kwang Won Park

Approved by:

(Chairman)

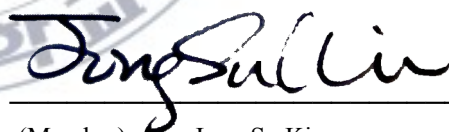
Yeon Tae Jeong

(Member)

Yong Seok Jeong

(Member)

Jong Su Kim

A handwritten signature in black ink, reading "Jong Su Kim", positioned over a horizontal line.

February 25, 2010

감사의 글

먼저 지난 5 년간의 발광연구실 과정 속에서 끊임없는 사랑과 믿음으로 도저히 할 수 없을 거라 생각했던 불가능의 것들을 가능하도록 내재된 열정을 불러일으켜주시고 새로운 세상의 문을 열 수 있는 기회와 “The show must go on”의 의지를 심어 주신, 저의 살아있는 역사이자 인생이신 김종수 교수님께 머리숙여 깊은 사랑과 감사를 드립니다. 학부 시절부터 멀리 보고 그 목표를 향해 현실에 최선을 다하라는 격려와 지도의 말씀을 아끼지 않으신 정연태 교수님, 존재의 이유만으로 힘이 되어주신 임권택 교수님, 보이지 않는 곳에서도 항상 따뜻한 관심으로 지켜봐 주시고 철저한 자기관리의 중요성을 일깨워주신 김종태 교수님, 저의 어리석음을 깨우쳐주시고 여유와 씬 또한 학업의 연장선임을 가르쳐주신 허훈 교수님, 대장부의 포부로 격려해주신 김지홍 교수님, 넉넉한 미소로 지켜봐 주시는 오정수 교수님, 때로는 따뜻한 조언으로 때로는 날카로운 비판으로 저를 돌아보게 해주신 정용석 교수님께 감사드립니다.

저를 믿고 무한한 기회와 가능성의 길을 열어주신 루시미아 전성덕 사장님, 충무공의 패기와 열정을 심어주신 한선규 이사님, “never give up”이란 일침과 깊은 관심으로 회사에 큰 힘이 되어주신 한국 하우톤 김광순 회장과 부족한 저를 항상 친형처럼 맞이해주시고 독려해주신 한국하우톤 김두명 전무님께 깊은 감사의 마음을 전합니다. 영광체의 현장과 현실을 일깨워주신 경북대학교 첨단디스플레이센터 김태훈 박사님, 어려운 상황 속에도 끝까지 함께 해주신 무진 권영규 사장님, 먼발치에서 실험실 지원사격을 아끼지 않으시는 한국기술교육대학교 김광철 교수님과 유중학 교수님께 감사드립니다. 또한, 늘 따뜻한 관심으로 함께해 주시는 인쇄정보공학과 이상남교수님과 손봉균 실장님, 바쁜 스케줄 속에서도 매번 측정에 도움을 주시는 손세모 교수님, 이태훈 박사님, 공동실험실습관의 김동우 선생님께 깊은 감사를 드립니다.

고통과 자학의 생활 일삼으며 연구에 매진하고 열정으로 치료하는 우리 발광연구실 식구들, 무중박사 박재홍, 신뢰성 있는 실험을 고집 할 줄 아는 신복 최남식, 허리띠 치켜올리며 무박 5 일의 실험강행을 마다치 않는 익덕 서광일, 실험에 감이 있는 박부원과 볼수록 알기 힘든 이성훈, 힘든 막내 생활로 여기 저기 뛰어다니기 바쁜 야망있는 이제범을 비롯해 이미지시스템공학과 선후배님 및 동기들 모두에게 감사드립니다.

이 작은 결실이 있기까지 흔들리지 않고 한 길을 갈 수 있도록 믿음 하나로 지켜봐 주시고 마음의 안식처가 되어주신 어머니 아버지와 한걸음 한걸음의 디딤돌이 되어주신 윤희누나, 광철이형, 자형, 형수님, 지친 일상 속에 큰 기쁨이 되어주는 우리조카 가을이, 영서, 은성이에게 깊은 사랑을 전합니다.

2009 년 12 월

“一切唯心造”

박 광 원

CONTENTS

Abstract	i
1. Introduction	1
2. Background	5
2.1. Phosphors for White-Light-Emitting Diodes	5
2.2. Luminescent properties of Ce^{3+} , Eu^{2+} , and Mn^{2+} ions	8
3. Experimental Procedure	12
3.1. Phosphor synthesis	12
3.2. Measurements of Phosphor properties	12
4. Results and Discussions	14
4.1 Structure of $\text{Ba}_{1.2}\text{Ca}_{0.8}\text{SiO}_4$ in binary Ba_2SiO_4 - Ca_2SiO_4 systems	14
4.2. $\text{Ba}_{1.2}\text{Ca}_{0.8-2x}\text{SiO}_4:x\text{Ce}^{3+}$, $x\text{Li}^+$	16
4.3. $\text{Ba}_{1.2}\text{Ca}_{0.8-2x-y}\text{SiO}_4:x\text{Ce}^{3+}$, $x\text{Li}^+$, $y\text{Mn}^{2+}$	23
4.4. The mixtures of $\text{Ba}_{1.2}\text{Ca}_{0.8-2x-y}\text{SiO}_4:x\text{Ce}^{3+}$, $x\text{Li}^+$, $y\text{Mn}^{2+}$ and $\text{Ba}_{1.2}\text{Ca}_{0.7}\text{SiO}_4:0.10\text{Eu}^{2+}$	32
5. Conclusions	37
References	39
국문요약	42

LIST OF FIGURES

Fig. 1. Tree types of white LEDs: (a) RGB individual LEDs; (b) blue LED and YAG:Ce yellow phosphor; (c) n-UV LED and white phosphor.	7
Fig. 2. The effect of the crystal field interaction on the (degenerate) free Ce^{3+} energy states. The combination of centroid shift and crystal field splitting decreases the lowest $5d$ state with a total energy D . On the far right the Stokes shifted $5d-4f$ emission transitions are shown.	9
Fig. 3. Schematic diagram of the energies of $4f^7$ and $4f^65d^1$ levels in Eu^{2+} influenced by crystal field Δ	9
Fig. 4. Energy level diagram for the d^5 configuration.	11
Fig. 5. A flow chart of phosphor synthesis by solid-state reaction.	13
Fig. 6. XRD patterns of $(\text{Ba}, \text{Ca})_2\text{SiO}_4:0.1\text{Ce}^{3+}/\text{Li}^+, 0.06\text{Mn}^{2+}$ with varying Ba/Ca composition ratio. ...	15
Fig. 7. Crystal structure of $\text{Ba}_{1.3}\text{Ca}_{0.7}\text{SiO}_4$	15
Fig. 8. XRD patterns (a) and the zoom-in (204) peaks (b) of $\text{Ba}_{1.20}\text{Ca}_{0.8-2x}\text{SiO}_4:x\text{Ce}^{3+}/\text{Li}^+$ with varying Ce^{3+} concentrations.	17
Fig. 9. PLE spectrum monitored at 400 nm of $\text{Ba}_{1.20}\text{Ca}_{0.60}\text{SiO}_4:0.10\text{Ce}^{3+}/\text{Li}^+$ phosphor.	18
Fig. 10. PL spectra (a) and PL intensities (b) of $\text{Ba}_{1.20}\text{Ca}_{0.8-2x}\text{SiO}_4:x\text{Ce}^{3+}/\text{Li}^+$ with varying Ce^{3+} concentration.	20
Fig. 11. Temperature-dependent PL spectra (a), PL intensities (b), and color coordinates (c) of $\text{Ba}_{1.20}\text{Ca}_{0.60}\text{SiO}_4:0.10\text{Ce}^{3+}/\text{Li}^+$ phosphor.	22
Fig. 12. XRD patterns of $\text{Ba}_{1.20}\text{Ca}_{0.8-2x-y}\text{SiO}_4:x\text{Ce}^{3+}/\text{Li}^+, y\text{Mn}^{2+}$ with varying Ce^{3+} ($x = 0.02, 0.06, 0.08,$ 0.10) (a) and Mn^{2+} concentration ($y = 0.02, 0.06, 0.08, 0.10$) (c). (b) and (d) show	

the zoom-in (204) peaks, respectively.	24
Fig. 13. PL spectra (a), enlarged PL spectra of Ce^{3+} (c) and enlarged PL spectra of Mn^{2+} (d) of $\text{Ba}_{1.20}\text{Ca}_{0.6-y}\text{SiO}_4:0.10\text{Ce}^{3+}/\text{Li}^+, y\text{Mn}^{2+}$ with varying Mn^{2+} concentration ($y = 0, 0.02, 0.04, 0.06, 0.08, 0.10$). (b) shows the 400 nm and 600 nm-monitored PLE spectra of the sample with $x=0.10$ and $y= 0.06$	26
Fig. 14. PL spectra (a) and color coordinates (b) of $\text{Ba}_{1.20}\text{Ca}_{0.74-2x}\text{SiO}_4:x\text{Ce}^{3+}/\text{Li}^+, 0.06\text{Mn}^{2+}$ with varying Ce^{3+} concentration ($x = 0.02, 0.04, 0.06, 0.08$). Enlarged PL spectra of Ce^{3+} (d) and Mn^{2+} (d). The inset of (a) shows the 400 nm and 600 nm-monitored PLE spectra of the sample with $x=0.10$ and $y= 0.06$	28
Fig. 15. EPR spectra (a) and enlarged EPR spectra (b) of $\text{Ba}_{1.20}\text{Ca}_{0.74-2x}\text{SiO}_4:x\text{Ce}^{3+}/\text{Li}^+, 0.06\text{Mn}^{2+}$ with varying Ce^{3+} concentration ($x = 0.02, 0.04, 0.06, 0.08, 0.10$).	29
Fig. 16. PL decay times for Mn^{2+} emissions of $\text{Ba}_{1.20}\text{Ca}_{0.74-2x}\text{SiO}_4:x\text{Ce}^{3+}/\text{Li}^+, 0.06\text{Mn}^{2+}$ with varying Ce^{3+} concentration ($x = 0.02, 0.04, 0.06, 0.08, 0.10$).	30
Fig. 17. Temperature-dependent PL spectra (a), PL intensity (b) and color coordinates (c) from $\text{Ba}_{1.20}\text{Ca}_{0.54}\text{SiO}_4:0.10\text{Ce}^{3+}, 0.10\text{Li}^+, 0.06\text{Mn}^{2+}$ excited at 365 nm.	31
Fig. 18. PL emission spectra (a), integrated PL intensities (b) and PL emission peak color coordinates (c) from $\text{Ba}_{1.20}\text{Ca}_{0.8-x}\text{SiO}_4:x\text{Eu}^{2+}$ with varying Eu^{2+} concentration ($x=0.02, 0.04, 0.06, 0.08, 0.10, 0.12$). PLE spectrum monitored at 480 and 510 nm from a $\text{Ba}_{1.20}\text{Ca}_{0.70}\text{SiO}_4:0.10\text{Eu}^{2+}$ phosphor (d). ...	32
Fig. 19. Normalized emission spectra (a)~(e) and color coordinates (f) of the mixtures of $\text{Ba}_{1.20}\text{Ca}_{0.74-2x}\text{SiO}_4:x\text{Ce}^{3+}/\text{Li}^+, 0.06\text{Mn}^{2+}$ and $\text{Ba}_{1.20}\text{Ca}_{0.70}\text{SiO}_4:0.10\text{Eu}^{2+}$ with changing their mixture ratio.	34
Fig. 20. Temperature-dependent PL spectra (a), PL intensities (b) and color coordinates (c) of the mixtures of $\text{Ba}_{1.20}\text{Ca}_{0.54}\text{SiO}_4:0.1\text{Ce}^{3+}/\text{Li}^+, 0.06\text{Mn}^{2+}$ and $\text{Ba}_{1.20}\text{Ca}_{0.70}\text{SiO}_4:0.10\text{Eu}^{2+}$	36

LIST OF TABLES

Table 1. Lattice constants and volumes of $\text{Ba}_{1.20}\text{Ca}_{0.8-2x}\text{SiO}_4:x\text{Ce}^{3+}/\text{Li}^+$ with varying Ce^{3+} concentration. When $a=0.573$, $c=14.58$ and space group of $P\bar{3}m1(164)$, $Z=4$	18
Table 2. Peak positions, widths and integrated PL intensity of PL spectra of $\text{Ba}_{1.20}\text{Ca}_{0.8-2x}\text{SiO}_4:x\text{Ce}^{3+}/\text{Li}^+$ with varying Ce^{3+} concentration.	21
Table 3. Peak positions of PL spectra of $\text{Ba}_{1.20}\text{Ca}_{0.6-y}\text{SiO}_4:0.10\text{Ce}^{3+}/\text{Li}^+$, $y\text{Mn}^{2+}$ with varying Mn^{2+} concentration ($y = 0, 0.02, 0.04, 0.06, 0.08, 0.10$)	26
Table 4. Peak positions of PL spectra of $\text{Ba}_{1.20}\text{Ca}_{0.74-2x}\text{SiO}_4:x\text{Ce}^{3+}/\text{Li}^+$, 0.06Mn^{2+} with varying Ce^{3+} concentration ($x = 0.02, 0.04, 0.06, 0.08, 0.10$)	28
Table 5. Color-rendering indices, correlated color temperature and color coordinate of the mixtures of $\text{Ba}_{1.20}\text{Ca}_{0.74-2x}\text{SiO}_4:x\text{Ce}^{3+}/\text{Li}^+$, 0.06Mn^{2+} and $\text{Ba}_{1.20}\text{Ca}_{0.70}\text{SiO}_4:0.10\text{Eu}^{2+}$ with changing their mixture ratio.	35

A Study on T-phase Phosphor in Binary Ba_2SiO_4 - Ca_2SiO_4 Systems for White-Light-Emitting Diode

Kwang Won Park

Department of Image System Science and Engineering,

The Graduate School,

Pukyong National University

Abstract

T-phase phosphors were developed in binary Ba_2SiO_4 - Ca_2SiO_4 systems activated by trivalent cerium, divalent europium, and divalent manganese and their luminescence characteristics were studied for phosphor-converted white-light-emitting diodes application. For the binary Ba_2SiO_4 - Ca_2SiO_4 systems, the (α'_L , α'_H , α , β , γ , T, X) phase transition occurs depending on the firing temperature and the composition variation of Ba/Ca, and they have diverse crystal structure orthorhombic, monoclinic, and hexagonal. In the region of $\text{Ba}_{1.2}\text{Ca}_{0.8}\text{SiO}_4 - \text{Ba}_{0.8}\text{Ca}_{1.2}\text{SiO}_4$, a T-phase structure belonged to the space group $P\bar{3}m1$ with hexagonal unit cell ($a = 0.573$ nm and $c = 0.729$ nm for the $\text{Ba}_{1.20}\text{Ca}_{0.80}\text{SiO}_4$) is confirmed. The following phosphors have developed for high-quality white-light generation; (i) $\text{Ba}_{1.2}\text{Ca}_{0.8-2x}\text{SiO}_4:\text{xCe}^{3+}/\text{Li}^+$ as a novel blue phosphor, (ii) deep-blue and red-emissive $\text{Ba}_{1.2}\text{Ca}_{0.8-2x-y}\text{SiO}_4:\text{xCe}^{3+}/\text{Li}^+, \text{yMn}^{2+}$ phosphor, and (iii) The mixtures of the blue/red-emissive $\text{Ba}_{1.2}\text{Ca}_{0.74-2x}\text{SiO}_4:\text{xCe}^{3+}/\text{Li}^+, 0.06\text{Mn}^{2+}$ and the green-emissive $\text{Ba}_{1.2}\text{Ca}_{0.7}\text{SiO}_4:0.1\text{Eu}^{2+}$. $\text{Ba}_{1.2}\text{Ca}_{0.8-2x}\text{SiO}_4:\text{xCe}^{3+}/\text{Li}^+$ phosphor exhibits two absorption bands at 280 nm and 325 nm, and an intense blue emission peaking at 400 nm. With increasing Ce/Li concentration, the lattice expands and the emission peak is blueshifted. This correlation is explained in terms of the crystal field effect and the configurational coordinate diagram. This phosphor shows much high thermal quenching temperature (225 °C) due to a weak electron-phonon interaction. $\text{Ce}^{3+}/\text{Mn}^{2+}$ -codoped T-phase $(\text{Ba}, \text{Ca})_2\text{SiO}_4$ phosphor shows two emission bands peaking at around 600 nm (red) and 400 nm (deep-blue) from the forbidden $^4T_1-^6A_1$ transition of Mn^{2+} ions and the allowed $4f-5d$ transition of Ce^{3+} ions, respectively. The strong interaction between Ce^{3+} and Mn^{2+} ions is investigated in terms of energy transfer, crystal field effect, and microstructure by changing their concentration. The correlation between decay times and electron paramagnetic resonance signals of Mn^{2+} ions demonstrates that local distortion around Mn^{2+} sites are influenced by the doped Ce^{3+} ions which violate their selection rule. They show much higher quenching temperature (250 °C) than junction temperature (125 °C) of light-emitting diode. Finally, high-quality white-light generation is achieved through both $\text{Ce}^{3+}/\text{Mn}^{2+}$ -doubly doped and Eu^{2+} -singly doped $(\text{Ba}, \text{Ca})_2\text{SiO}_4$ phosphors. The mixtures, excited by the near-ultraviolet of 365 nm, show the various qualities of white lights depending on the mixture ratio; the correlated color-temperatures from 3500 to 7000 K, and the color-rendering indices up to 95 %.

Keywords: $(\text{Ba}, \text{Ca})_2\text{SiO}_4:\text{Ce}^{3+}$, Mn^{2+} phosphor, Crystal field, Energy Transfer, Thermal quenching, White-light-emitting diode.

1. INTRODUCTION

Conventional lamps rely on either incandescence or discharge in gases. Both phenomena are associated with large energy losses that are essentially inherent because of the high temperatures and large Stokes shifts involved. The development of visible and near-ultraviolet (n-UV) light-emitting diodes (LEDs) that exhibit efficiencies comparable or higher than those of conventional lamps gave birth to new lighting technology^[1-1].

Such a development of LEDs has stimulated research on phosphors used for white LEDs (W-LED). Solid-state lighting using LEDs and phosphors material have its impact in reducing the global electricity consumption. The strategies involved in developing W-LED are (i) the combination of blue, green, and red LEDs; (ii) the combination of a blue LED with a yellow phosphor; and (iii) the combination of UV-LED with blue, green, and red phosphors.

A white LED composed of a blue InGaN-based LED and a yellow-emitting $\text{Y}_3\text{Al}_5\text{O}_{12}:\text{Ce}^{3+}$ (YAG:Ce) was first commercialized by NICHIA co. in 1996^[1-2, 3]. Since introduction of W-LED with this type, phosphor-converted LEDs (pc-LEDs) known as the “blue-YAG white”, has captured a substantial market because of their attractive properties such as reduced power consumption, compactness, efficient light output, reliability, nonpollution and longer lifetime^[1-4]. These pc-LEDs have been rapidly developed over the last few years. With recent technological advances, the application of pc-LEDs has shifted from display to lighting, as they are increasingly being used as solid-state lighting sources and devices that have the same lighting properties as conventional incandescent bulbs and fluorescent lamps.

However, the color-rendering indices of the conventional technology based on blue-YAG white LEDs are about 80, and low-color temperatures around 3000 K cannot be attained by this system. Even though blue-YAG white LEDs are enough for general illumination, it is usually not acceptable for high-quality white lighting such as certain domestic lighting use and architectural lighting purposes due to the poor performance of the red component in the spectra.

Accordingly, one of the main current scientific issues is in the development of low color-temperature, high color-rendering and thermally stable phosphors for domestic lighting use and architectural lighting purposes^[1-5]. The high-color rendering properties can be achieved by using full-color white phosphor and

UV LED ^[1-6]. The white LEDs based on UV LED and full color RGB phosphor are superior to “blue-YAG white LED” in some respects; their high color-rendering performance in general household lighting applications, their uniformity in the emitted white color, and wider chromaticity are some of the apparent advantages. However, despite of the abundance of the red color, these phosphors using UV LED still show practically significant change in white-color qualities with increasing temperatures of LED. Namely, their variations in emission intensity and color coordinates against operating temperature are too large for them to be applied to white LEDs ^[1-7]. In addition, they are composed of more than four components, causing the formation of some undesired phases.

Therefore, it is necessary to develop of high-quality phosphors corresponding to the household lighting demands. The properties required by the phosphor for high-quality W-LED acceptable for domestic use and architectural lighting purposes may include the following attributes:

- It should have high quantum efficiency when emitting light of the desired wavelength.
- High color-rendering indices (CRIs) over 85% are acceptable for domestic use.
- It should be chemically stable over its entire operating temperature range and over the lifespan of the pcLED.
- Its emission intensity in the visible should not be drastically temperature dependent over the operating temperature range. Many LEDs that may have the phosphor applied in the LED package in front of the emitting surface reach temperatures of 125 °C or more, and the phosphor must be an efficient emitter at such temperatures. Ideally it should be stable to at least 200 °C.
- It should have a good particle morphology and narrow particle size distribution for easy incorporation into silicones or epoxy resins.
- It needs to have its grain size optimized to reduce/eliminate scattering.
- For many of these properties, it is necessary to optimize the phosphor composition and crystallinity.

Here, this study has focused on research and development to find the appropriate phosphor corresponding to the above requirements: high quantum efficiency, high color-rendering indices, low-color temperature, and thermally stable property. To survey n-UV or deep blue LED-excitable phosphor with high

efficiency and excellent color-rendering index for white LED, the best way is to extend the studies on the efficiency-proven existent phosphors.

The codoping into $(\text{Ba, Sr, Ca})_2\text{SiO}_4:\text{Eu}^{2+}$ phosphor can give a new approach to satisfy the requirements. Although Eu^{2+} -doped $(\text{Ba, Ca, Sr})_2\text{SiO}_4$ phosphors have been reported for several decades and extensively used as a high efficient green-yellow phosphor for color conversion in blue InGaN-based W-LED, limited color-rendering indices and low thermal quenching temperature still remain controversial. Also, despite of easy prospect on additional red emission through Mn^{2+} codoping into $(\text{Ba, Sr, Ca})_2\text{SiO}_4$ host lattice, there have been few reports regarding Mn^{2+} luminescence in $(\text{Ba, Sr, Ca})_2\text{SiO}_4$ host lattice.

The spectroscopic properties of Mn^{2+} ions are strongly influenced by their surrounding environments, and they prefer to substitute the four or six-coordinated sites on which they give a strong emission ^[1-8-10]. According to this idea, we have tried to search for the host structure with Mn^{2+} -substitutive four or six-coordinated cation sites in the $\text{Ba}_2\text{SiO}_4\text{-Ca}_2\text{SiO}_4\text{-Sr}_2\text{SiO}_4$ systems ^[1-11]. For the binary $\text{Ba}_2\text{SiO}_4\text{-Ca}_2\text{SiO}_4$ systems, the $(\alpha'_L, \alpha'_H, \alpha, \beta, \gamma, T, X)$ phase transition occurs depending on the firing temperature and the composition variation of Ba/Ca, and so they have diverse crystal structure orthorhombic, monoclinic, and hexagonal. In the region of $\text{Ba}_{1.2}\text{Ca}_{0.8}\text{SiO}_4\text{--Ba}_{0.8}\text{Ca}_{1.2}\text{SiO}_4$, a T-phase structure belonged to the space group $P\bar{3}m1$ with hexagonal unit cell ($a = 0.573$ nm and $c = 0.729$ nm for the $\text{Ba}_{1.20}\text{Ca}_{0.80}\text{SiO}_4$) is confirmed. $\text{Ba}_{1.2}\text{Ca}_{0.8}\text{SiO}_4$ host lattice has a unique crystal structure with Mn^{2+} ions-substitutive four or six-coordinated cation sites and the red emission from Mn^{2+} ions is possible only for these T-phase $(\text{Ba, Ca})_2\text{SiO}_4$ host lattice in binary $\text{Ba}_2\text{SiO}_4\text{-Ca}_2\text{SiO}_4$ systems.

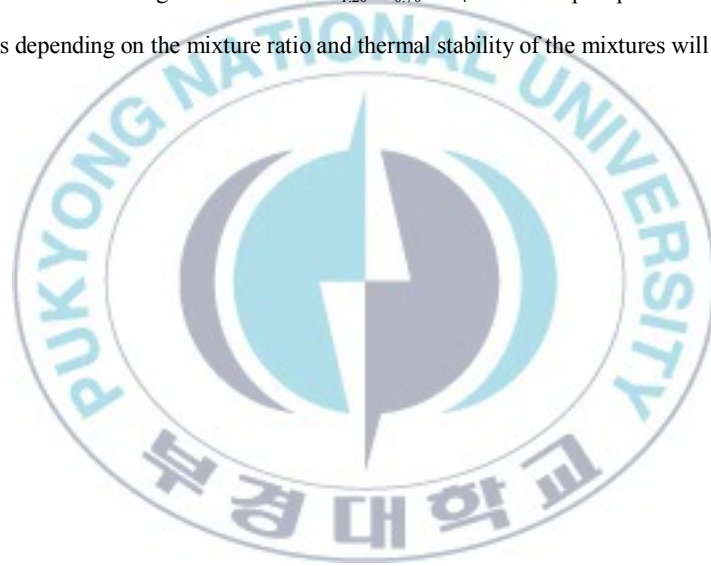
In this work, T-phased phosphors activated by Ce^{3+} , Eu^{2+} , and Mn^{2+} in binary $\text{Ba}_2\text{SiO}_4\text{-Ca}_2\text{SiO}_4$ systems are developed to meet the above requirements for high-quality W-LED and why the red emission from Mn^{2+} ions is possible only for T-phase $(\text{Ba, Ca})_2\text{SiO}_4$ host lattice will be revealed. T-phased phosphors developed in binary $\text{Ba}_2\text{SiO}_4\text{-Ca}_2\text{SiO}_4$ systems are as following items.

(1) A novel blue phosphor, $\text{Ba}_{1.2}\text{Ca}_{0.8-2x}\text{SiO}_4:x\text{Ce}^{3+}/\text{Li}^+$, has been developed for W-LED. The phosphor exhibits two absorption bands at 280 nm and 325 nm, and an intense deep-blue emission peaking at 400 nm. The microstructural and spectroscopic variations caused by doping Ce ions will be investigated in terms of

the crystal field effect and the configurational coordinate diagram. Furthermore, the temperature dependence of emission intensity will be measured.

(2) An innovative deep-blue and red-emissive T-phase $\text{Ba}_{1.20}\text{Ca}_{0.8-2x-y}\text{SiO}_4:x\text{Ce}^{3+}/\text{Li}^+, y\text{Mn}^{2+}$ phosphor has been developed to meet the above requirements for white-light quality. T-phase $\text{Ba}_{1.3}\text{Ca}_{0.7}\text{SiO}_4$ host lattice is one of the most chemically stable structure over all combinations of Ba_2SiO_4 - Ca_2SiO_4 - Sr_2SiO_4 systems^[1-12]. However, its potential as a UV-excited phosphor has not been demonstrated. Here, the strong interaction between $\text{Ce}^{3+}/\text{Mn}^{2+}$ ions is investigated in terms of energy transfer, crystal field effect, and microstructure by changing their concentration. The thermal stability of the phosphor is also examined.

(3) Finally, to improve the color-rendering index of T-phase $\text{Ba}_{1.20}\text{Ca}_{0.8-2x-y}\text{SiO}_4:x\text{Ce}^{3+}, x\text{Li}^+, y\text{Mn}^{2+}$, its blending with the isostructural green-emissive $\text{Ba}_{1.20}\text{Ca}_{0.70}\text{SiO}_4:0.10\text{Eu}^{2+}$ phosphor has been investigated. Optical properties depending on the mixture ratio and thermal stability of the mixtures will be investigated.



2. BACKGROUND

2.1. Phosphors for White-LEDs

Presently three kinds of white LEDs have been proposed and constructed, as follows:

1. Three LEDs of the primary colors are combined with each other.
2. A yellow phosphor or two phosphors (red and green) are mounted on a blue LED.
3. A combination of two or more phosphors, spanning the blue to red spectrum, is applied to a UV or violet LED (365–420 nm).

The device structures of three types W-LEDs as described above are schematically shown in Figure 1. Although it is possible to obtain a full spectrum of colors from III-V LEDs and related compounds, there are a number of problems associated with LEDs. The RGB approach (Figure 1. (a)) requires at least three LEDs, and each device must be adjusted by individual supply circuits to balance the emission intensity of each color for proper white light generation because of varying brightness of the different wavelength emitting LEDs. This is known as the Green Window problem, and is caused by the lack of good external quantum efficiency, EQE, values in the deep green to yellow region of the spectrum since each illuminance distribution is different, it is very difficult to produce a mixed homogeneous white light. These can be readily addressed by using a phosphor-conversion LED.

In 1991, Nichia Corporation pioneered the development of blue LEDs based on InGaN. This invention already raised the concept of an LED combined with a phosphor as was seen in a patent issued at this period [2-1]. It was 1996 when a W-LED composed of a blue LED and a yellow-emitting $\text{Y}_3\text{Al}_5\text{O}_{12}:\text{Ce}^{3+}$ (YAG:Ce) was first commercialized (Figure 1. (b)). The combination of blue and yellow light gives the sensation of white color by the principle of complementary colors. Since their introduction, this type of white LEDs, known as the “blue-YAG white”, has captured a substantial market because of their attractive properties such as reduced power consumption, compactness, efficient light output, reliability, nonpollution and longer lifetime. However, several problems that currently exist with blue-YAG white LEDs. These include the halo effect of blue/yellow color separation, strong temperature and current dependence of chromaticity, and poor color rendering due to the lack of green and red components. A light source requires high-quality light

radiation because when we look at objects we see the reflected light. The spectrum of the illumination source affects the appearances of objects, producing the phenomenon we call color rendering. If the illumination source does not induce a spectrum close to that of incandescent bulbs or the Sun, then the color of objects will be different from what we are accustomed to. If we can match the appropriate multicolor phosphor and encapsulation material to the n-UV region, then we can obtain white LEDs with both high-color rendering and high luminous efficacy.

In the past few years, high-power UV LEDs have been developed by a number of companies and institutions. This has stimulated the research and development of phosphors, which can be excited by UV LEDs, emitting the three primary colors, blue, green, and red; white LEDs as well as devices emitting intermediate colors can then be obtained with the proper admixture of these tricolor phosphors. The white-LEDs based on UV LEDs are superior to “blue-YAG white” in some respects; their high color-rendering performance in general illumination applications, their uniformity in the emitted white color, and wider chromaticity of backlight for liquid crystal displays are some of the apparent advantages. The n-UV white LED approach (Figure 1. (c)) is analogous to three-color fluorescent lamp technology, which is based on the conversion of n-UV radiation to visible light via the photoluminescence process in phosphor materials. In the blue/YAG process, a sharp blue light from the blue LED source is an essential component of white light, and is strongly affected by temperature and drive current. UV light, on the other hand, is not included in the white light generation from n-UV-based devices. This technology can thus provide a higher quality of white light compared to the blue YAG method. Accordingly, we can design emission color with large flexibility using a wide selection and combination of phosphors, particularly white with high color-rendering index and an expanded range of color in the chromaticity diagram for backlighting of liquid crystal displays. The system has the additional advantage that its emission chromaticity depends little on the amount of phosphors mounted on the LED chip, because in principle the phosphors used absorb most of the UV- or n-UV emissions. Consequently, variation of LED emission color can be reduced.

Recently many reports and patents have been published on yellow phosphors other than YAG:Ce, for example thiogallates, silicates, nitrides, and oxynitrides activated mostly with Eu^{2+} [2-2-9]. As for emission color other than yellow, a red-emitting nitride phosphor, $(\text{Sr,Ca})_2\text{Si}_3\text{N}_8:\text{Eu}^{2+}$, was developed and warm-white LEDs using this compound and YAG:Ce deposited on a blue LED was commercialized in 2003. This

technology has led to the production of white LEDs with high color-rendering index, the average index R_a being above 90, at any color temperature. This is generally accomplished by adding a red component (phosphor) to the emission spectrum of conventional “blue-LED YAG.” The development of these warm-white LEDs has led to their applications in general purpose illumination like meeting household lighting demands. Since the development of $(\text{Sr}, \text{Ca})_2\text{Si}_5\text{N}_8:\text{Eu}^{2+}$, a variety of phosphors including other nitrides have been developed. Development of red-emitting nitride phosphors has solved the problem of high color-rendering light sources. However, current manufacturing processes of the nitride phosphors are not suited to mass production. To meet the predicted large demand for such LEDs, a new process to synthesize the required phosphors simply and economically in a large scale will need to be developed. For the backlighting of liquid crystal displays, which forms a growing market, a combination of UV LEDs and phosphors emitting in three primary colors presents us with a challenging problem.

In this study, the mixtures of the blue/red-emissive $(\text{Ba}, \text{Ca})_2\text{SiO}_4:\text{Ce}^{3+}, \text{Mn}^{2+}$ and the green-emissive $(\text{Ba}, \text{Ca})_2\text{SiO}_4:\text{Eu}^{2+}$, excited by the near ultraviolet of 365 nm, show the various qualities of white lights depending on the mixture ratio; the correlated color-temperatures from 3500 to 7000 K, and the color-rendering indices up to 95 %. Furthermore, it shows very high thermal quenching temperature (225 °C)

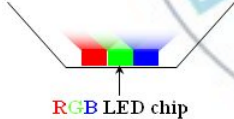
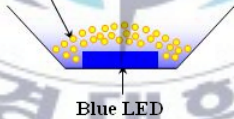
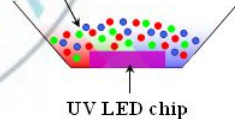
All semiconductor-based illumination devices	Semiconductor/phosphor devices	
(a) R+G+B LED Chip	(b) Blue LED Chip + Yellow phosphor	(c) UV Chip + RGB phosphor
 <p>RGB LED chip</p>	 <p>Yellow phosphor + Epoxy/Silicon</p> <p>Blue LED</p>	 <p>RGB phosphor + Epoxy/Silicon</p> <p>UV LED chip</p>
<ul style="list-style-type: none"> • Potentially highest efficiency • Very large color gamut • Tunable white point 	<ul style="list-style-type: none"> • The most simple technology • Decent color rendering ($R_a \sim 80$) 	<ul style="list-style-type: none"> • White point determined by phosphors only • Excellent color rendering
<ul style="list-style-type: none"> • Green LED efficiency is low • Temperature stability of LEDs depends on color • Individual supply circuits 	<ul style="list-style-type: none"> • Reduced extraction efficiency • “Quantum deficit” is fundamental • Blue LED + YAG phosphor: High CCT and limited color rendering • UV LED + RGB phosphor: Degradation of organic encapsulants 	

Fig. 1. Three types of white LEDs: (a) RGB individual LEDs; (b) blue LED and YAG:Ce yellow phosphor; (c) n-UV LED and white phosphor

2.2. Luminescent properties of Ce^{3+} , Eu^{2+} , and Mn^{2+} ion

(1) Ce^{3+}

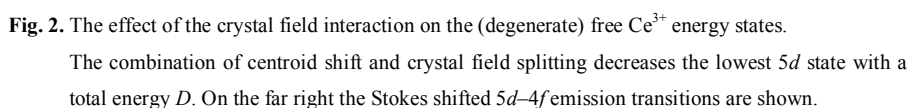
Ce^{3+} ion ($4f^1$) is the most simple example, since it is a one-electron case. The excited configuration is $5d^1$. The $4f^1$ ground state configuration yields two levels, viz. $^2F_{5/2}$ and $^2F_{7/2}$, separated by some 2000cm^{-1} due to spin-orbital coupling. The $5d^1$ configuration is split by the crystal field in 2 to 5 components. The total splitting amounts to some 15000cm^{-1} (Fig.2). The luminescence photon energy depends strongly on the structure of the host crystal through the crystal-field splitting of the $5d$ state, as shown in Figure 2 and varies from near-ultraviolet to the greenish yellow region. The emission occurs from the lowest crystal field component of the $5d^1$ configuration to the two levels, $^2F_{5/2}$ and $^2F_{7/2}$, of the ground state. This gives the Ce^{3+} emission its typical double-band shape.

The decay time of the Ce^{3+} emission is 10^{-7} to 10^{-8} s, the shortest in observed lanthanide ions. This is due to two reasons: the $d \rightarrow f$ transition is both parity-allowed and spin allowed since $5d^1$ and $4f^1$ states are spin doublets, i.e., the emission transition is a fully allowed one [2-10]. The decay time is longer if the emission is at longer wavelengths: 20 ns for the 300 nm emission of CeF_3 , and 70 ns for 550 nm emission of $Y_3Al_5O_{12}:Ce^{3+}$. It can be derived that for a given transition the decay time τ is proportional to the square of the emission wavelength λ [2-11]: $\tau \sim \lambda^2$.

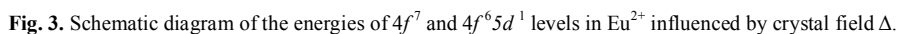
The Stokes shift of the Ce^{3+} emission is never very large and varies from a thousand to a few thousand wave numbers (medium coupling case). The spectral position of the emission band depends on three factors:

- covalency (nephelauxetic effect) which will reduce the energy difference between the $4f^1$ and $5d^1$ configurations.
- crystal field splitting of the $5d^1$ configuration: a large low-symmetry crystal field will lower the lowest crystal-field component from which the emission originates.
- the Stokes shift.

Usually the Ce^{3+} emission is in the ultraviolet of blue spectral region, but in $Y_3Al_5O_{12}$ it is in the green and red (crystal-field effect), and in CaS in the red (nephelauxetic effect).



The electronic configuration of Eu^{2+} is $4f^7$. The lowest excited state of $4f$ levels, ${}^6\text{P}_j$, is higher than the $4f^6 5d^1$ level in most crystals, so that Eu^{2+} usually gives broad-band emission due to f - d transitions. The d -orbital is fivefold degenerate in free space. In crystal some symmetry it is split into a threefold degenerate $d\varepsilon$ -orbitals and twofold degenerate $d\gamma$ -orbitals. The wavelength positions of the emission bands depend very much on hosts, changing from the near-UV to the red. This dependence is interpreted as due to the crystal field splitting of the $5d$ level, as shown schematically in Figure 3 [2-12]. With increasing crystal field strength, the emission bands shift to longer wavelength. The luminescence peak energy of the $5d$ - $4f$ transitions of Eu^{2+} and Ce^{3+} are affected most by crystal parameters denoting electron-electron repulsion.



The blue luminescence (450 nm) in BaMgAl₁₀O₁₇ is used for three-band fluorescent lamps. Greenish-yellow luminescence (560 nm) in (Ba, Sr)₂SiO₄ and red luminescence (650nm) in CaAlSiN₃ are used for GaN based W-LED, respectively. Red luminescence (650nm) is also observed in Eu²⁺-activated CaS [2-13]; the crystal field is stronger in sulfides and nitrides than in fluorides and oxides.

The lifetime of the Eu²⁺ luminescence is 10⁻⁵–10⁻⁶ s, which is relatively long for an allowed transition. This is due to the fact that the ground state of 4f⁷ is ⁸S, and the multiplicity of the excited state 4f⁶5d¹ is 6 or 8; (spin) the sextet portion of the excited state contributes to the spin-forbidden character of the transition, so that the spin selection rule slows down the optical transition rate [2-10].

(3) Mn²⁺

The Mn²⁺ ion has an emission which consists of a broad band, the position of which depends strongly on the host lattice. The emission can vary from green (490 nm) to deep red (750 nm). The decay time of this emission is of the order of ms.

From the Tanabe-Sugano diagram (Fig. 4) the emission corresponds to the ⁴T₁(4G) → ⁶A₁(6S) transition is derived. When a metal ion occupies a certain position in a crystal, the crystal field strength that affects the ion increases as the space containing the ion becomes smaller, as expected from Eq. (2-29). For increases in the field, the transition energy between the ⁴T₁ and ⁶A₁ levels is predicted to decrease (shift to longer wavelengths). In fact, the peak wavelength of the Mn²⁺ luminescence band is known to vary linearly to longer wavelength (547 to 602 nm) with a decrease in Mn-F distance (2.26 to 1.99Å) in a group of fluorides, including 10 perovskite lattices of the type AB^{II}F₃, ZnF₂, and MgF₂. A similar relationship also holds for each group of oxo-acid salt phosphors having an analogous crystal structure; the wavelength is longer when Mn²⁺ replaces a smaller cation in each group. On the other hand, a larger anion complex makes the cation space shrink, leading to longer-wavelength luminescence. For Ca₁₀(PO₄)₆F₂:Mn²⁺, the crystal field at a Mn²⁺ ion produced by ions in eight unit cells around it was calculated theoretically. The result was consistent with the observed luminescence peak shift (100 cm⁻¹) to longer wavelength due to a lattice constant decrease (0.14%) when one Ca in each Ca₁₀(PO₄)₆F₂ is replaced by Cd.

In spite of the fact that the ionic radius for Zn²⁺ (0.72 Å) is smaller than that for Ca²⁺ (0.99 Å), the luminescence wavelength in Zn₂SiO₄:Mn²⁺ is shorter than in CaSiO₃:Mn²⁺. This is attributed to a smaller

coordination number (4) in the former as compared with that (6) in the latter. In materials containing a spinel structure, Mn^{2+} can occupy either octahedral or tetrahedral sites. From the fact that the luminescence occurs in the shorter-wavelength (green) region, the tetrahedral site is expected to be occupied preferentially by Mn^{2+} . This is confirmed by ESR and ion-exchange studies for β -aluminas and supported by thermodynamic data.

In $\text{CaF}_2:\text{Mn}^{2+}$, though Mn^{2+} occupies a cubic site with high coordination number, Dq is not so large because the anion valency of F^- is smaller than that of O^{2-} . In addition, B is large because of the smaller nephelauxetic effect. Consequently, this compound yields the shortest luminescence wavelength (~ 495 nm) observed among Mn^{2+} -doped phosphors.

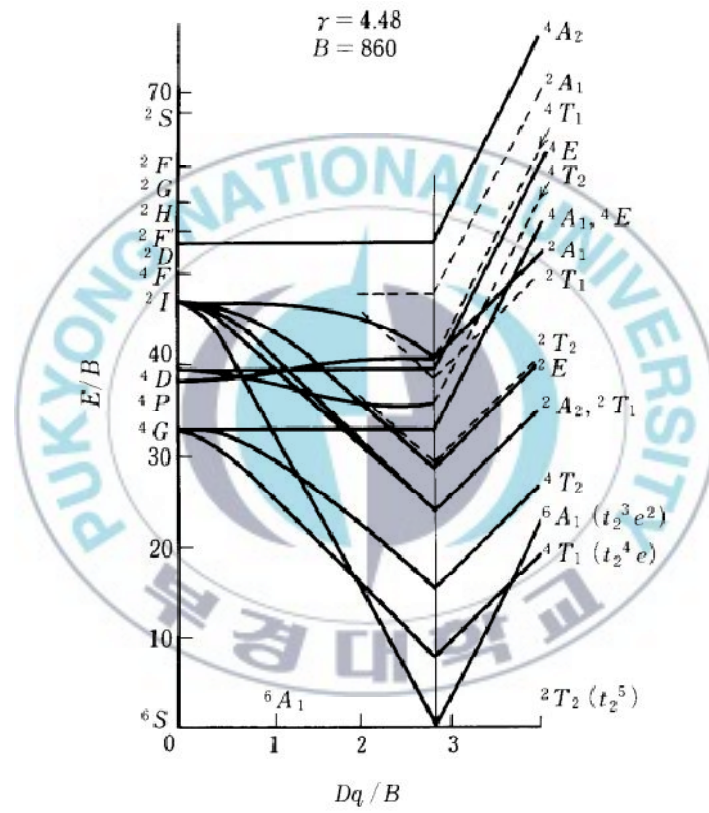


Fig. 4. Energy level diagram for the d^5 configuration.

3. EXPERIMENTAL PROCEDURE

3.1. Phosphor synthesis

As shown in Fig. 5, for the preparation of $\text{Ba}_{1.20}\text{Ca}_{0.8-2x}\text{SiO}_4:\text{xCe}^{3+}/\text{Li}^+$ phosphors, reagent-grade BaCO_3 , CaCO_3 , SiO_2 , CeO_2 , and Li_2O as a charge compensator were mixed in the molar ratio of 1.2 : 0.8-2x : 1 : x : x/2, respectively. Also for the preparation of $\text{Ba}_{1.20}\text{Ca}_{0.8-2x-y}\text{SiO}_4:\text{xCe}^{3+}$, xLi^+ , yMn^{2+} phosphors, reagent-grade BaCO_3 , CaCO_3 , SiO_2 , CeO_2 , Li_2O , Eu_2O_3 and MnO were weighed in the molar ratio of 1.2: 0.8-2x-y: 1: x: x/2: y. Stoichiometric amounts of the starting materials were thoroughly mixed in a ball mill with a small amount of zirconia beads and ethanol for 12 hours. And then the slurry was dried in oven at 85°C for 24 hours. Subsequently, all samples were fired through a conventional solid-state reaction technique. The synthesis was performed at 1200°C for 4 hours in a reducing atmosphere (a mixture of 5% H_2 and 95% N_2) in an electric furnace. In the firing steps the temperature was gradually raised ($5^\circ\text{C}/\text{min}$) until the final temperature was reached. After these steps the temperature was slowly lowered to room temperature.

The final formulation $\text{Ba}_{1.20}\text{Ca}_{0.8-2x}\text{SiO}_4:\text{xCe}^{3+}/\text{Li}^+$ and $\text{Ba}_{1.20}\text{Ca}_{0.8-2x-y}\text{SiO}_4:\text{xCe}^{3+}$, xLi^+ , yMn^{2+} samples were prepared with changing Ce^{3+} , $\text{Ce}^{3+}/\text{Mn}^{2+}$ and Eu^{2+} concentrations in steps of 0.02 mole. Also the isostructural $\text{Ba}_{1.20}\text{Ca}_{0.7}\text{SiO}_4:0.10\text{Eu}^{2+}$ phosphor was sintered by the same process for a green-color compensator.

- (1) $\text{Ba}_{1.20}\text{Ca}_{0.8-2x}\text{SiO}_4:\text{xCe}^{3+}/\text{Li}^+$ (0.04 $\leq x \leq 0.14$, 0.02 steps)
- (2) $\text{Ba}_{1.20}\text{Ca}_{0.8-2x-y}\text{SiO}_4:\text{xCe}^{3+}$, xLi^+ , yMn^{2+} (0 $\leq x \leq 0.10$, 0.02 $\leq y \leq 0.10$, 0.02 steps)
- (3) $\text{Ba}_{1.20}\text{Ca}_{0.8-z}\text{SiO}_4:\text{zEu}^{2+}$ (0.02 $\leq z \leq 0.12$)
- (4) The mixtures of $\text{Ba}_{1.20}\text{Ca}_{0.7}\text{SiO}_4:0.10\text{Eu}^{2+}$ and $\text{Ba}_{1.20}\text{Ca}_{0.8-2x-y}\text{SiO}_4:\text{xCe}^{3+}$, xLi^+ , yMn^{2+} (1:10 \leq mixture ratio \leq 1:50)

3.2. Measurements of Phosphor properties

The obtained phosphors were identified through X-ray diffraction (XRD) technique ($\text{Cu K}\alpha$, D/MAX 2500) with Ni-filtered $\text{Cu-K}\alpha$ radiation, counting times of 30 minutes from 20° to 80° and 2 θ steps of 0.02° . To confirm the fine structural variation in the local environment of Mn^{2+} site due to Ce^{3+} doping, electron paramagnetic resonance (EPR) was measured with a Bruker ESP-300E spectrometer working at X-band at

room temperature. The photoluminescence (PL) and photoluminescence excitation (PLE) spectra were obtained using Hitachi F-4500 fluorescence spectrometer. Their color coordinates and color temperatures, and color rendering indices were measured in the reflection mode at room temperature using a 365 nm mercury lamp as an excitation source and PR-650 SpectraScan spectroradiometer as a detector.

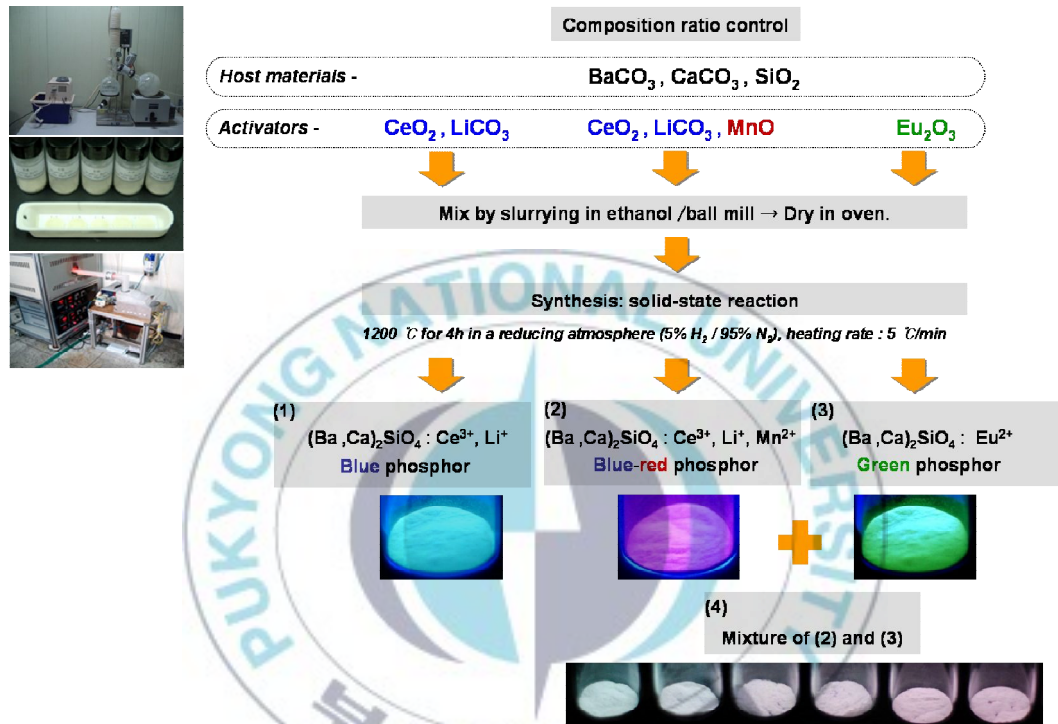


Fig. 5. A flow chart of phosphor synthesis by solid-state reaction.

4. RESULTS AND DISCUSSIONS

4.1 Structure of $Ba_{1.2}Ca_{0.8}SiO_4$ host lattice in binary Ba_2SiO_4 - Ca_2SiO_4 systems

For the binary Ba_2SiO_4 - Ca_2SiO_4 systems, the (α'_L , α'_H , α , β , γ , T, X) phase transition occurs depending on the firing temperature and the composition variation of Ba/Ca, and they have diverse crystal structure orthorhombic, monoclinic, hexagonal [4-1-3]. In this work, the only phase with Mn^{2+} ions-substitutive four or six-coordinated cation sites in many polymorphic modifications (α'_L , α'_H , α , β , γ , T, X) of the binary Ba_2SiO_4 - Ca_2SiO_4 systems was found.

Figure 6 shows XRD patterns of $(Ba, Ca)_2SiO_4:0.1Ce^{3+}/Li^+$, $0.06Mn^{2+}$ with varying Ba/Ca composition ratios at the fixed Ce ($x = 0.10$) and Mn ($y = 0.06$) concentrations.. XRD patterns in the region of $Ba_{1.2}Ca_{0.8}SiO_4$ - $Ba_{0.8}Ca_{1.2}SiO_4$ match well with JCPDS card #36-1449, and is identified as T phase whereas the others are identified as α , β , γ phase in the order of increasing Ca compositions. In the region of $Ba_{1.2}Ca_{0.8}SiO_4$ - $Ba_{0.8}Ca_{1.2}SiO_4$, a new T-phase structure belonged to the space group $P\bar{3}m1$ with hexagonal unit cell ($a = 0.573$ nm and $c = 0.729$ nm for the $Ba_{1.20}Ca_{0.80}SiO_4$) is confirmed. The T phase is built up of five Ba/Ca sites (one $M(2)O_6$ octahedra, four $MO(1, 3, 4, 5)_{10 \text{ or } 12}$ polyhedra) and two SiO_4 tetrahedral sites (Fig. 7) [4-2]. Each site has the following site occupancy of Ba and Ca ions; M1: 60.65% Ba and 39.35% Ca; M2: 78.65% Ba and 21.35% Ca; M3: 91.57% Ba and 8.43% Ca; M4: 2.22% Ba and 97.78% Ca; M5: 100% Ba. It is known that any dopants are preferentially substituted for the sites to minimize the mismatches in size and coordination number. The Mn^{2+} ion has a preferential occupancy of six-coordinated Ca^{2+} sites, i.e., M(2) site occupied by Ca^{2+} ion [4-4-6]. The Ce^{3+} ion has a relatively high coordination number of more than 6 and it is in the middle size of Ca^{2+} and Ba^{2+} ions so that it can statistically occupy one of four M(1, 3, 4, 5) sites [4-1, 2].

Especially only T phase in the binary Ba_2SiO_4 - Ca_2SiO_4 systems has a single octahedral Ba/Ca site with 6-coordination number, whereas other systems including pure Ba_2SiO_4 and Ca_2SiO_4 compounds have two different Ba/Ca polyhedrons with more than 9-coordination number.

According to this context, the intense Mn^{2+} emission is possible only for the host lattice with octahedral or tetrahedral cation sites, i.e., only octahedrally-coordinated Mn^{2+} ion into T phase $(Ba, Ca)_2SiO_4$ lattice in

the binary Ba_2SiO_4 - Ca_2SiO_4 systems can show the Mn^{2+} emission. Especially, the phases in the region of $\text{Ba}_{1.2}\text{Ca}_{0.8}\text{SiO}_4$ - $\text{Ba}_{0.8}\text{Ca}_{1.2}\text{SiO}_5$ show the most intense Ce and Mn emissions.

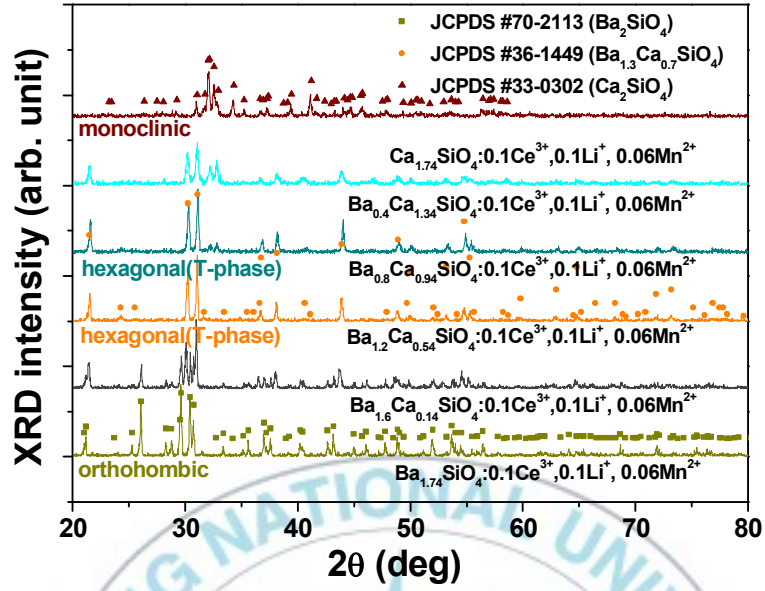


Fig. 6. XRD patterns of $(\text{Ba}, \text{Ca})_2\text{SiO}_4:0.1\text{Ce}^{3+}/\text{Li}^+, 0.06\text{Mn}^{2+}$ with varying Ba/Ca composition ratio.

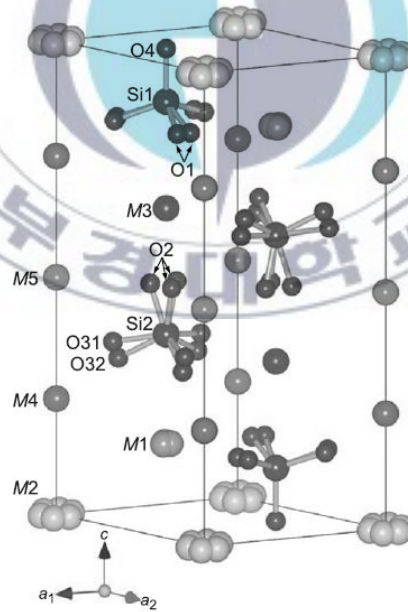


Fig. 7. Crystal structure of $\text{Ba}_{1.3}\text{Ca}_{0.7}\text{SiO}_4$.

4.2. $Ba_{1.2}Ca_{0.8-2x}SiO_4:xCe^{3+}, xLi^+$

Figure 8 (a) shows XRD patterns of $Ba_{1.20}Ca_{0.8-2x}SiO_4:xCe^{3+}/Li^+$ with varying Ce^{3+} concentrations. XRD patterns of all samples match well with JCPDS card #36-1449, indicating that all samples are a single phase called T phase^[4-3]. The T phase belongs to the space group $P\bar{3}m1$ with hexagonal unit cell. The T-phase is built up of five Ba^{2+}/Ca^{2+} sites (one $M(2)O_6$ ring and four $M(1, 3, 4, 5)O_{10/12}$ polyhedrons) and two SiO_4 tetrahedral sites^[4-1]. Each site has the following site occupancy of Ba and Ca ions; M1: 65.7% Ba and 34.3% Ca; M2: 85.2% Ba and 14.8% Ca; M3: 99.2% Ba and 0.8% Ca; M4: 2.4% Ba and 97.6% Ca; M5: 100%.

As an increase of Ce ions, all peaks are shifted to the smaller-angle side, and then return to the larger-angle side as seen in figure 8 (b) and Table 1, indicating that the lattices expand along with increasing Ce ions, and then they shrink; $a = 5.7605 \text{ \AA}$ and $c = 14.7033 \text{ \AA}$ for $x=0.04$, $a = 5.7666 \text{ \AA}$ and $c = 14.8245 \text{ \AA}$ for $x=0.10$, $a = 5.7666 \text{ \AA}$ and $c = 14.7092 \text{ \AA}$ for $x=0.12$. It is known that any dopants are preferentially substituted for the sites to minimize the mismatches in size (ionic radii for 6-coordinate and 8-coordinate; Ca^{2+} : 114 pm and 126 pm, Ba^{2+} : 149 pm and 156 pm, Ce^{3+} : 115 pm and 128 pm, Li^+ : 90 pm and 106 pm, respectively). As a result of the lattice constants, it can be considered that, at Ce concentrations of less than $x=0.10$, Ce/Li ions occupy Ca ions of five Ba/Ca sites, leading to the lattice expansion, and then at Ce concentrations of more than $x=0.10$, Ce/Li ions occupy Ba ions as well as Ca ions of five Ba/Ca sites, causing to the decrease of lattice constants on average. It follows well the formulation $Ba_{1.20}Ca_{0.8-2x}Ce_xLi_xSiO_4$, which is designed for Ce/Li ions to be substituted for Ca ions.

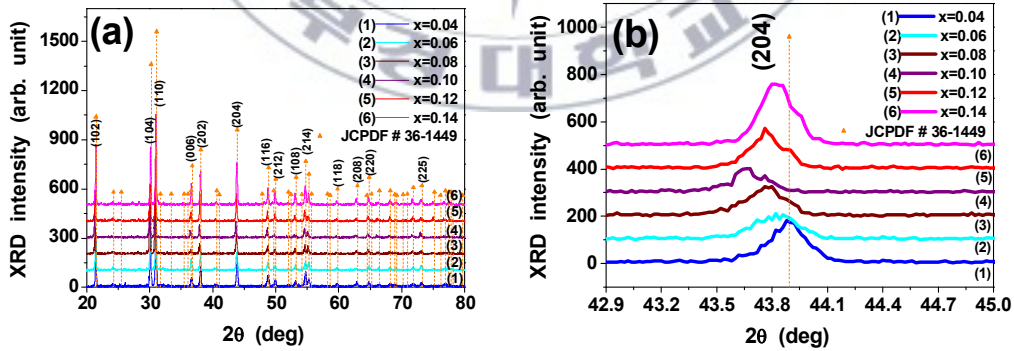


Fig. 8. XRD patterns (a) and the zoom-in (204) peaks (b) of $Ba_{1.20}Ca_{0.8-2x}SiO_4:xCe^{3+}/Li^+$ with varying Ce^{3+} concentration.

Table 1. Lattice constants and volumes of $\text{Ba}_{1.20}\text{Ca}_{0.8-2x}\text{SiO}_4:x\text{Ce}^{3+}/\text{Li}^+$ with varying Ce^{3+} concentration.
When $a=0.573$, $c=14.58$ and space group of $P\bar{3}m1(164)$, $Z=4$

Ce^{3+} Mole(%)	$a = b$	c	$\text{Vol}(\text{\AA}^3)$
4	5.76057	14.70335	422.55
6	5.75731	14.68238	421.47
8	5.77085	14.69970	423.95
10	5.76668	14.82455	426.94
12	5.76662	14.70925	423.61
14	5.75991	14.70277	422.44

The PLE spectrum of $\text{Ba}_{1.20}\text{Ca}_{0.60}\text{SiO}_4:0.10\text{Ce}^{3+}/\text{Li}^+$ phosphor is depicted in Figure 9. The PLE spectrum monitored at 400 nm for the $\text{Ba}_{1.20}\text{Ca}_{0.60}\text{SiO}_4:0.10\text{Ce}^{3+}/\text{Li}^+$ phosphor shows the characteristic doublet of Ce^{3+} ion. The excitation bands at 280 nm and 325 nm correspond to the transitions of 5d states to $^2F_{5/2}$ and $^2F_{7/2}$ of Ce^{3+} ion, respectively [4-7].

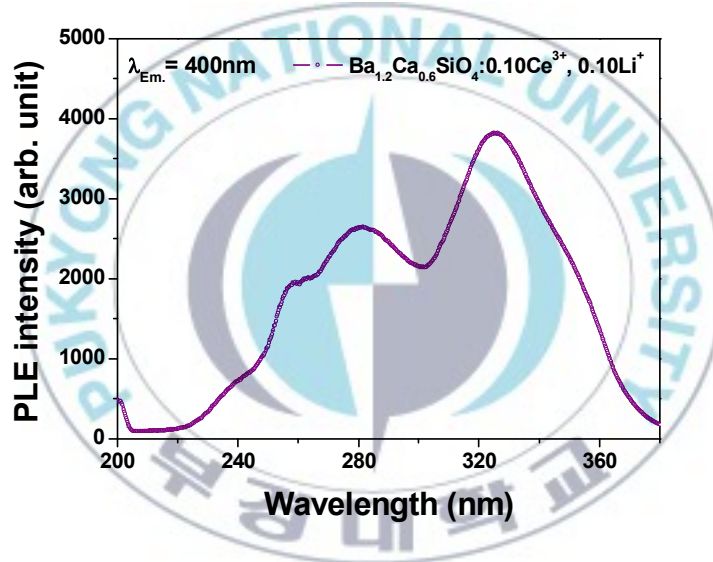


Fig. 9. PLE spectrum monitored at 400 nm of $\text{Ba}_{1.20}\text{Ca}_{0.60}\text{SiO}_4:0.10\text{Ce}^{3+}/\text{Li}^+$ phosphor.

The PL spectra of $\text{Ba}_{1.20}\text{Ca}_{0.8-2x}\text{SiO}_4:x\text{Ce}^{3+}/\text{Li}^+$ with varying Ce^{3+} concentrations are depicted in Fig. 10 (a). The characteristic doublet of Ce^{3+} ion is not clearly observed in the emission spectrum. The PL spectra exhibit a broad blue emission band peaking at 400 nm with a half width of 80 nm due to the allowed $f-d$ transition in Ce^{3+} ions [4-7]. The PL spectra result from the spectral overlap of five different emission peaks

associated with Ce^{3+} ions substituted for five Ba/Ca sites in the T phase. As shown in Fig. 10 (b), the PL intensity increases with Ce^{3+} contents increasing until a maximum intensity of about $x = 0.10$ is reached, and then it decreases due to the concentration quenching process. According to Ref. [4-8], the critical transfer distance (R_c) of Ce^{3+} in $\text{Ba}_{1.20}\text{Ca}_{0.60}\text{SiO}_4:0.10\text{Ce}^{3+}/\text{Li}^+$ phosphor is approximately calculated to be 11.76 Å, which is far more than the typical critical distance of 5 Å enough to trigger the exchange interaction between different Ce^{3+} ions. It indicates that the energy transfer process between different Ce^{3+} ions, which is responsible for the quenching process, is controlled by not exchange interaction but electric multipole–multipole interaction.

As shown in Table 2, with increasing Ce^{3+} concentration, the PL spectra are gradually blueshifted; peak positions: 413.6 nm for $x = 0.04$ and 395.2 nm for $x = 0.12$. It can be understood in terms of the crystal field theory [4-9]. The crystal field strength is influenced by site symmetry, covalency, ligand charge and bond length. Among these parameters, the bond length (R) affects the crystal field strength (Dq) significantly, i.e., Dq is proportional to $1/R^5$. The Ce^{3+} ion on the site with the shorter bond length experiences the higher crystal field, which causes to lowering the excited states and decreasing their transition energy. As mentioned, Ce/Li ions are replaced for Ca ions, resulting in the increase of the lattice constants, i.e., the bond lengths. Consequently the crystal field strengths are reduced along with increasing Ce/Li ions so that the emission peaks are blueshifted.

Also, with increasing Ce^{3+} concentration, the PL spectra are gradually sharpening along with their gradual blueshifting; peak widths: 89.6 nm for $x = 0.04$ and 79.2 nm for $x = 0.10$. The spectral width is influenced by the measured temperature, and the energy and the number of phonons involved. The decreased Stokes shift due to substitution of Ce/Li ions means that the electron-phonon interaction is weakened, i.e., the energy and/or the number of phonons are decreased. This weak electron-phonon interaction causes to sharpening of the spectral width.

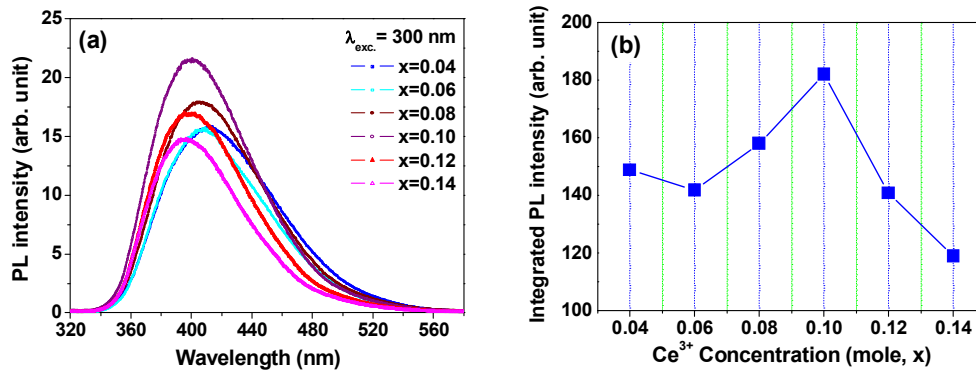


Fig. 10. PL spectra (a) and PL intensities (b) of $\text{Ba}_{1.20}\text{Ca}_{0.8-2x}\text{SiO}_4:x\text{Ce}^{3+}/\text{Li}^+$ with varying Ce^{3+} concentration.

Table 2. Peak positions, widths and integrated PL intensity of PL spectra of $\text{Ba}_{1.20}\text{Ca}_{0.8-2x}\text{SiO}_4:x\text{Ce}^{3+}/\text{Li}^+$ with varying Ce^{3+} concentration.

Ce^{3+} concentration (mole %)	Emission maximum (nm)	Emission peak's width (nm)	Integrated PL intensity
4	413.6	89.6	148715.4277
6	408.8	82.2	141816.2489
8	404.4	82.6	157968.3947
10	400.8	79.2	181982.9962
12	395.2	76.6	140731.2632
14	396.4	74.2	118945.4751

The temperature-dependent PL intensities of $\text{Ba}_{1.20}\text{Ca}_{0.6}\text{SiO}_4:0.10\text{Ce}^{3+}/\text{Li}^+$ phosphor excited at 365 nm are shown in Fig. 11 (b). The quenching temperature (T_q), at which the initial PL intensity is halved, is about 225 °C. This value is much higher than that of a commercial yellow $(\text{Ba}, \text{Sr})_2\text{SiO}_4:\text{Eu}^{2+}$ on a blue LED (150 °C) [4-10]. This excellent thermal stability can be explained by the configuration coordinate diagram [4-7]. A thermal activation energy increases with decreasing Stokes shift, leading to increasing the nonradiative barrier from the excited state to the ground state. Therefore, our deep-blue emissions with comparatively lower Stokes shift are weakly coupled with phonons so that they are slowly quenched at higher temperature.

In addition, the color coordinates move to the deeper-blue color region as a function of the temperature as seen in Fig. 11 (c). As mentioned, the broad emission spectrum is an overlapping result of five resolved peaks from Ce^{3+} ions substituted for five Ba/Ca sites. Among the five overlapped peaks, the longer-wavelength peak with larger Stoke shift might be faster quenched than the shorter-wavelength peak. In other

words, as an increase of temperature, the shorter-wavelength peak of all peaks is more dominant, and thus the color coordinates move to the deeper-blue color region.

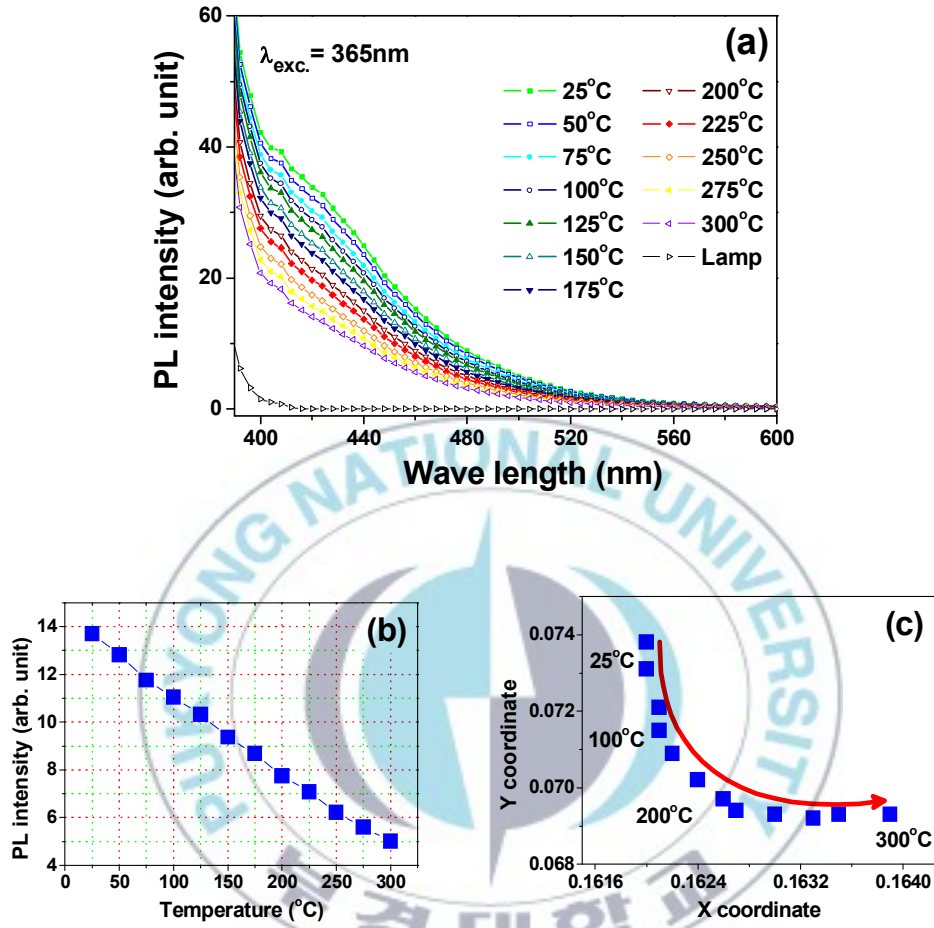


Fig. 11. Temperature-dependent PL spectra (a), PL intensities (b) and color coordinates (c) of $\text{Ba}_{1.20}\text{Ca}_{0.60}\text{SiO}_4:0.10\text{Ce}^{3+}/\text{Li}^{+}$ phosphor.

4.3. $Ba_{1.20}Ca_{0.8-2x-y}SiO_4:xCe^{3+}, xLi^+, yMn^{2+}$

Figure 12 shows XRD patterns of $Ba_{1.20}Ca_{0.8-2x-y}SiO_4:xCe^{3+}, xLi^+, yMn^{2+}$ with varying Ce^{3+}/Mn^{2+} concentrations. XRD patterns of all samples match well with JCPDS card #36-1449, indicating that all samples are a single phase called T phase. The T phase belongs to the space group $P\bar{3}m1$ with hexagonal unit cell. It consists of five Ba^{2+}/Ca^{2+} sites (one $M(2)O_6$ ring and four $M(1, 3, 4, 5)O_{10/12}$ polyhedrons) and two SiO_4 tetrahedral sites^[4-]. As an increase of Ce^{3+} ions, all peaks are shifted to the smaller-angle side (see Fig. 12 (b)). It indicates that the lattices expand along with increasing Ce^{3+} ions; $a = 5.74293 \text{ \AA}$ and $c = 14.65615 \text{ \AA}$ for $x=0.02$, and $a = 5.74681 \text{ \AA}$ and $c = 14.67277 \text{ \AA}$ for $x=0.08$. Accordingly, we can conclude that Ce^{3+}/Li ions occupy smaller Ca^{2+} ions of five Ba^{2+}/Ca^{2+} sites, leading to the lattice expansion. Contrary to addition of Ce^{3+} ions, with increasing Mn^{2+} ions, all peaks are shifted to the larger-angle side as seen in Fig. 12 (d). It implies that the lattices shrink along with increasing Mn^{2+} ions; $a = 5.75048 \text{ \AA}$ and $c = 14.67933 \text{ \AA}$ for $x=0.02$, and $a = 5.73648 \text{ \AA}$ and $c = 14.61587 \text{ \AA}$ for $x=0.10$. It is due to a substitution of smaller Mn^{2+} ions for larger Ca^{2+}/Ba^{2+} ions.

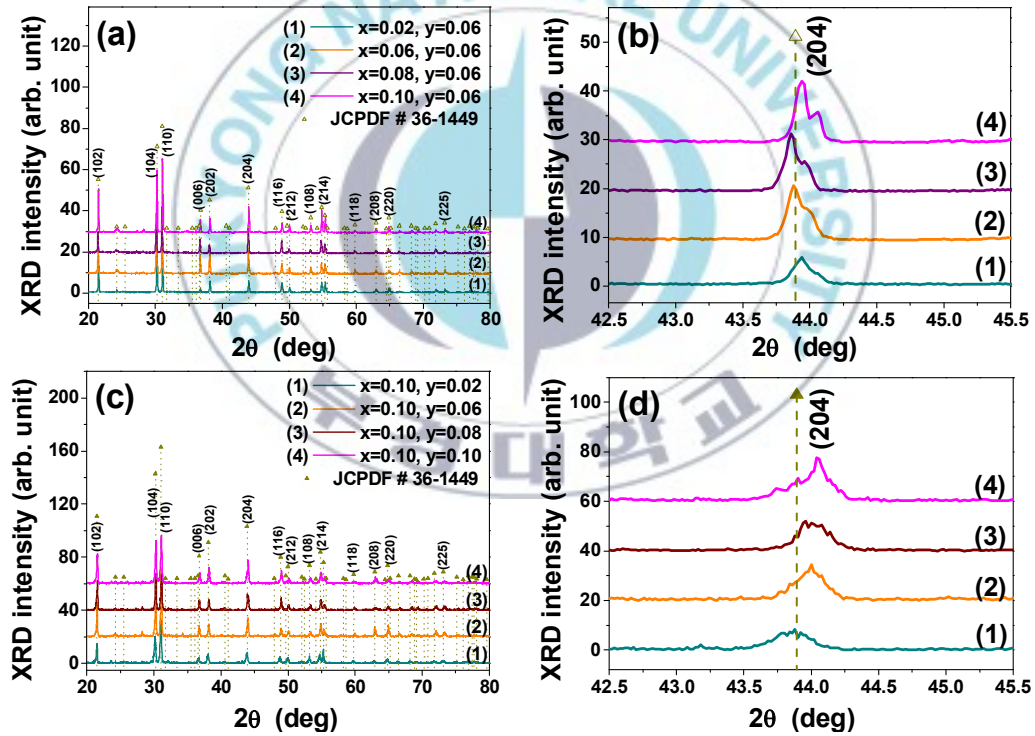


Fig. 12. XRD patterns of $Ba_{1.20}Ca_{0.8-2x-y}SiO_4:xCe^{3+}/Li^+, yMn^{2+}$ with varying Ce^{3+} concentration ($x = 0.02, 0.06, 0.08, 0.10$) (a) and Mn^{2+} concentration ($y = 0.02, 0.06, 0.08, 0.10$) (c). (b) and (d) show the zoom-in (204) peaks, respectively.

Figure 13 (a) shows PL spectra of $\text{Ba}_{1.20}\text{Ca}_{0.60-y}\text{SiO}_4:0.10\text{Ce}^{3+}, 0.01\text{Li}^+, y\text{Mn}^{2+}$ with varying Mn^{2+} concentrations at the fixed Ce^{3+} concentrations. All spectra consist of both the deep-blue and the red emission bands. The deep-blue emission bands are originated from the allowed $f-d$ transition of Ce^{3+} ions. The red emissions are attributed to the ${}^4\text{T}_1-{}^6\text{A}_1$ forbidden transitions of Mn^{2+} ions with a millisecond order of decay time. As seen in Fig. 13 (b), the PLE spectrum monitored at 400 nm shows the characteristic doublet of Ce^{3+} ion which corresponds to the transitions of 5d states to ${}^2\text{F}_{5/2}$ and ${}^2\text{F}_{7/2}$ of Ce^{3+} ion, respectively [4-7]. The PLE spectrum monitored at 600 nm shows the same as the Ce^{3+} PLE spectrum. It indicates that the Mn^{2+} emission is originated from the Ce^{3+} excitation. This is the other evidence on the energy transfer between Ce^{3+} and Mn^{2+} ions [4-5]. As seen in Fig. 13 (c) and (d), as an increase of Mn^{2+} concentrations (y), the deep-blue emission bands are significantly decreased whereas the red emission bands are increased to be maximized at $y = 0.08$, and then both bands are quenched due to the quenching effect in heavy doping. This behavior can be explained by the well-known energy transfer mechanism from the deep-blue Ce^{3+} emission band to the Mn^{2+} absorption band [4-7]. As an increase of y, the red emission band is redshifted by 12 nm: the peak at 589 nm for $y = 0.02$ and that at 601 nm peak for $y = 0.08$ (see Table 3). A substitution of smaller Mn^{2+} ions for Ca^{2+} sites can cause to decreasing the bond length. This shorter bond length leads to the increase of the crystal field strength which is inversely proportional to the bond length, and consequently the increased crystal field results in the redshift of the emission peak [4-4, 7].

Figure 14 shows PL spectra (a) and color coordinates (b) of $\text{Ba}_{1.20}\text{Ca}_{0.74-2x}\text{SiO}_4:x\text{Ce}^{3+}, x\text{Li}^+, 0.06\text{Mn}^{2+}$ with varying Ce^{3+} concentrations at the fixed Mn^{2+} concentrations. The deep-blue emission bands are decreased along with increasing of the red emission bands (see Fig. 14 (c) and (d)). It is based on the energy transfer between Ce^{3+} and Mn^{2+} ions. As an increase of $\text{Ce}^{3+}/\text{Li}^+$ (x), the deep-blue emission band is blueshifted by 21 nm (421 nm for $x = 0.02$, and 400 nm for $x = 0.10$) (see Table 4). It demonstrates that a substitution of larger Ce^{3+} ions for Ca^{2+} sites causes to an expansion of host lattice, and thus a decrease in the crystal field strength of Ce^{3+} ions. The peak shift of blue band from Ce^{3+} ions (~ 21 nm) along with increasing Ce^{3+} ions is more sensitive to Ce^{3+} contents than that of red band from Mn^{2+} ions (~ 2 nm). Also, an addition of Mn^{2+} ions causes to the larger redshift of Mn^{2+} emission (~ 12 nm) than that of Ce^{3+} emission (~ 4 nm). It can be considered that the dopants make a local variation in crystal field around themselves, but the crystal field effect is so weak to the other sites that the emission spectra of their codopants are slightly changed.

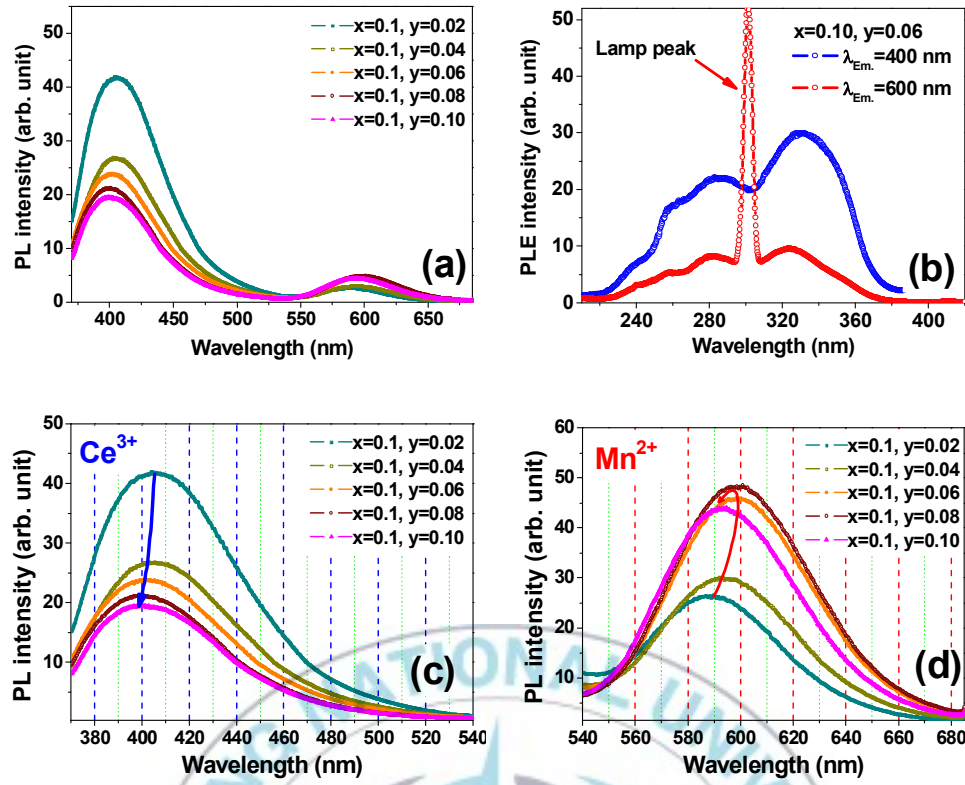


Fig. 13. PL spectra (a), enlarged PL spectra of Ce^{3+} (c) and Mn^{2+} (d) of $\text{Ba}_{1.20}\text{Ca}_{0.6-y}\text{SiO}_4:0.10\text{Ce}^{3+}/\text{Li}^+, y\text{Mn}^{2+}$ with varying Mn^{2+} concentration ($y = 0, 0.02, 0.04, 0.06, 0.08, 0.10$). (b) shows the 400 nm and 600 nm-monitored PLE spectra of the sample with $x=0.10$ and $y=0.06$.

Table 3. Peak positions of PL spectra of $\text{Ba}_{1.20}\text{Ca}_{0.6-y}\text{SiO}_4:0.10\text{Ce}^{3+}/\text{Li}^+, y\text{Mn}^{2+}$ with varying Mn^{2+} concentration ($y = 0, 0.02, 0.04, 0.06, 0.08, 0.10$)

x (mole)	y (mole)	Emission maximum (Ce^{3+}), nm	Emission maximum (Mn^{2+}), nm	Integrated intensity
0.1	0.02	404.2	589.6	377184.3942
0.1	0.04	402.6	592	263767.3298
0.1	0.06	400.8	599	251642.1414
0.1	0.08	400.2	601	229404.3003
0.1	0.1	399	594.6	211665.4129

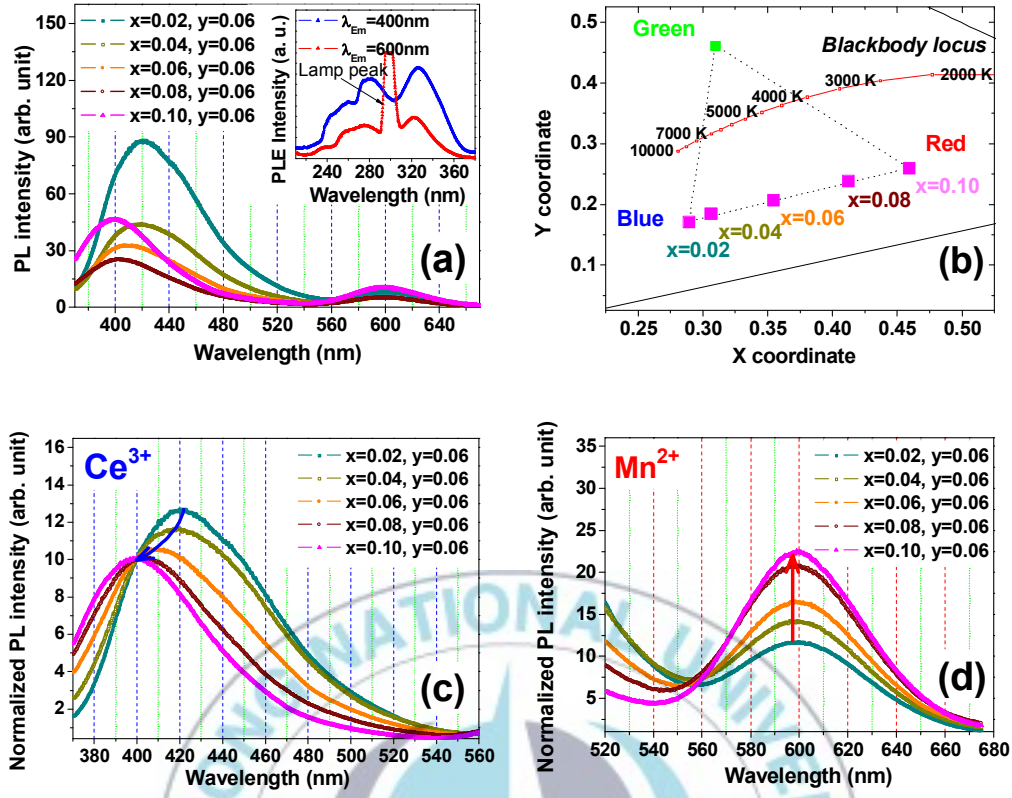


Fig. 14. PL spectra (a) and color coordinates (b) of $\text{Ba}_{1.20}\text{Ca}_{0.74-2x}\text{SiO}_4:x\text{Ce}^{3+}/\text{Li}^+, 0.06\text{Mn}^{2+}$ with varying Ce^{3+} concentration ($x = 0.02, 0.04, 0.06, 0.08, 0.10$). Enlarged PL spectra of Ce^{3+} (c) and enlarged PL spectra of Mn^{2+} (d). The inlet of (a) shows the 400 nm and 600 nm-monitored PLE spectra of the sample with $x=0.10$ and $y=0.06$.

Table 4. Peak positions of PL spectra of $\text{Ba}_{1.20}\text{Ca}_{0.74-2x}\text{SiO}_4:x\text{Ce}^{3+}/\text{Li}^+, 0.06\text{Mn}^{2+}$ with varying Ce^{3+} concentration ($x = 0.02, 0.04, 0.06, 0.08, 0.10$)

x (mole)	y (mole)	Emission maximum (Ce^{3+}), nm	Emission maximum (Mn^{2+}), nm	Integrated intensity
0.02	0.06	421	598.8	120.76875
0.04	0.06	418.6	596.2	118.62284
0.06	0.06	406.4	598.4	105.78694
0.08	0.06	403.2	600.4	97.72492
0.10	0.06	400	598.8	90.87401

For Mn^{2+} -singly doped samples without Ce^{3+} ions, the red emissions from Mn^{2+} ions are not observed. However, an addition of even a small amount of Ce^{3+} ions ($x = 0.01$) causes to the orders-of-magnitude enhancement of the red emission from Mn^{2+} ions. The similar phenomena were observed in other $\text{Eu}^{2+}/\text{Mn}^{2+}$ -codoped phosphors [4-11, 12]. Here we can suggest the simple reason why Ce^{3+} ions around Mn^{2+} sites can induce the slight influence on site symmetry of Mn^{2+} sites and the violation of Mn^{2+} selection rule so as to enhance Mn^{2+} emissions. To confirm the fine structural variation in the local environment of Mn^{2+} site due to Ce^{3+} doping, EPR spectra of $\text{Ba}_{1.20}\text{Ca}_{0.74-2x}\text{SiO}_4:x\text{Ce}^{3+}, x\text{Li}^+, 0.06\text{Mn}^{2+}$ were measured.

As seen in Fig. 15, all samples show a single broad resonance line due to Mn^{2+} - Mn^{2+} interaction-induced broadening effect [4-13]. As an increase of Ce^{3+} concentrations at a fixed Mn^{2+} concentration, the line widths are broadening and shifting to the higher-field side. It can be understood in terms of the fine structural variation in the local environment of Mn^{2+} , which is induced by Ce^{3+} doping. The Ce^{3+} ions can be locally inhomogeneous-distributed around Mn^{2+} sites, and thus force an asymmetric electric field to Mn^{2+} sites so as to distort their environments. Consequently this local distortion can cause to the degeneracy removal and the splitting of spin-energy levels of Mn^{2+} ions, and finally may give rise to the broader EPR spectrum along with the higher-magnetic-field side [4-13, 14]. This argument is supported by the variation in Mn^{2+} decay times along with increasing with Ce^{3+} ions.

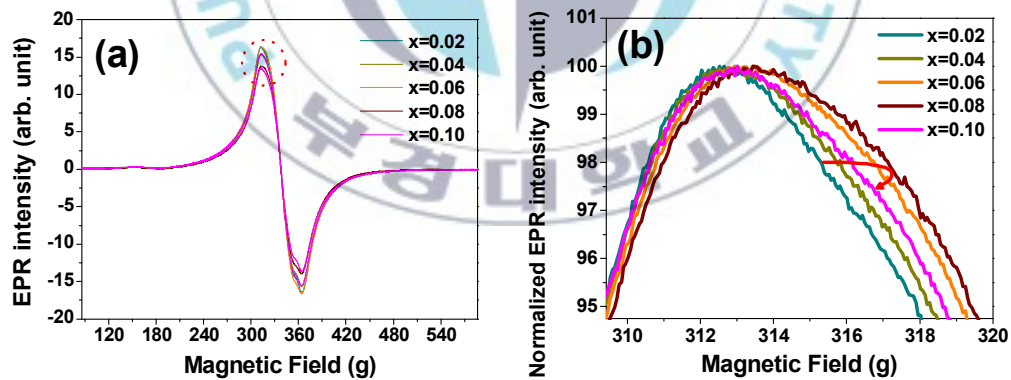


Fig. 15. EPR spectra (a) and enlarged EPR spectra (b) of $\text{Ba}_{1.20}\text{Ca}_{0.74-2x}\text{SiO}_4:x\text{Ce}^{3+}/\text{Li}^+, 0.06\text{Mn}^{2+}$ with varying Ce^{3+} concentration ($x = 0.02, 0.04, 0.06, 0.08, 0.10$).

The PL decay curves for the 610 nm red peaks of $\text{Ba}_{1.20}\text{Ca}_{0.74-2x}\text{SiO}_4:x\text{Ce}^{3+}, x\text{Li}^+, 0.06\text{Mn}^{2+}$ with increasing Ce^{3+} concentrations are represented in Fig. 16. The decay curve of the Ce^{3+} -sensitized Mn^{2+} acceptor ions can be expressed by [4-15];

$$N_A(t) = \frac{W_{DA}N_{D0}}{(P_A^r - P_D^r - W_{DA})} \times \{\exp[-(P_D^r + W_{DA})t] - \exp(-P_A^r t)\}$$

In this equation, W_{DA} is the energy transfer rate between Ce^{3+} donor and Mn^{2+} acceptor, and $N_A(t)$ and N_{D0} represent the population of the excited state of Mn^{2+} acceptor at the time t and the initial population of the excited state of Ce^{3+} donor immediately after the pulse, respectively, and P_D^r and P_A^r are the radiative rates of the Ce^{3+} donor and the Mn^{2+} acceptor which are equal to the inverses of the decay times. By performing simple simulation to predict the Mn^{2+} acceptor decay time, it is expected that as the P_D^r and the W_{DA} increase, the $N_A(t)$ increases at a given time; that is, the acceptor decay increases. However, our experimental result is contrary to the theoretical prediction. As an increase of the Ce^{3+} donor concentrations (x) at the fixed Mn^{2+} acceptor concentrations, the Mn^{2+} acceptor's decay times are gradually shortening from 23.3 ms at $x \approx 0.02$ to 21.6 ms at $x = 0.10$. This shortening of Mn^{2+} acceptor decay times can take place under the condition characterized by a local distortion of Mn^{2+} sites caused by Ce^{3+} doping, which is consistent with EPR results. It leads to a weakening of the ban on Mn^{2+} acceptor transitions so as to reduce Mn^{2+} acceptor decay times.

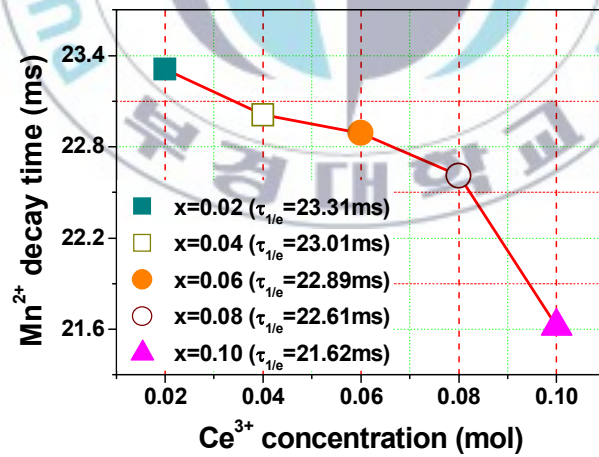


Fig. 16. PL decay times for Mn^{2+} emissions of $\text{Ba}_{1.20}\text{Ca}_{0.74-2x}\text{SiO}_4:x\text{Ce}^{3+}/\text{Li}^+, 0.06\text{Mn}^{2+}$ with varying Ce^{3+} concentration ($x = 0.02, 0.04, 0.06, 0.08, 0.10$).

The temperature-dependent PL spectra from $\text{Ba}_{1.20}\text{Ca}_{0.54}\text{SiO}_4:0.10\text{Ce}^{3+}, 0.10\text{Li}^+, 0.06\text{Mn}^{2+}$ excited at 365 nm (where the maximal excitation efficiency occurs) are shown in Fig. 17 (a). As seen in Figure 17(b), the T_q at which the initial PL intensity is halved, is about 250 °C for both emission colors which is comparable to that of a commercially used yellow-emitting $(\text{Ba}, \text{Sr})_2\text{SiO}_4:\text{Eu}^{2+}$ on a blue LED (150 °C) [4-16]. The peak positions in the red emission spectra are blueshifted with increasing temperature: from 620 nm at 25 °C to 600 nm at 250 °C. It leads to the shift of the color coordinates to the blue region as shown in Fig. 17 (c). This blueshift was commonly observed in many Eu^{2+} and Mn^{2+} doped-silicate phosphors, and explained by a phonon-assisted upconversion process called anti-Stokes shift [4-4].

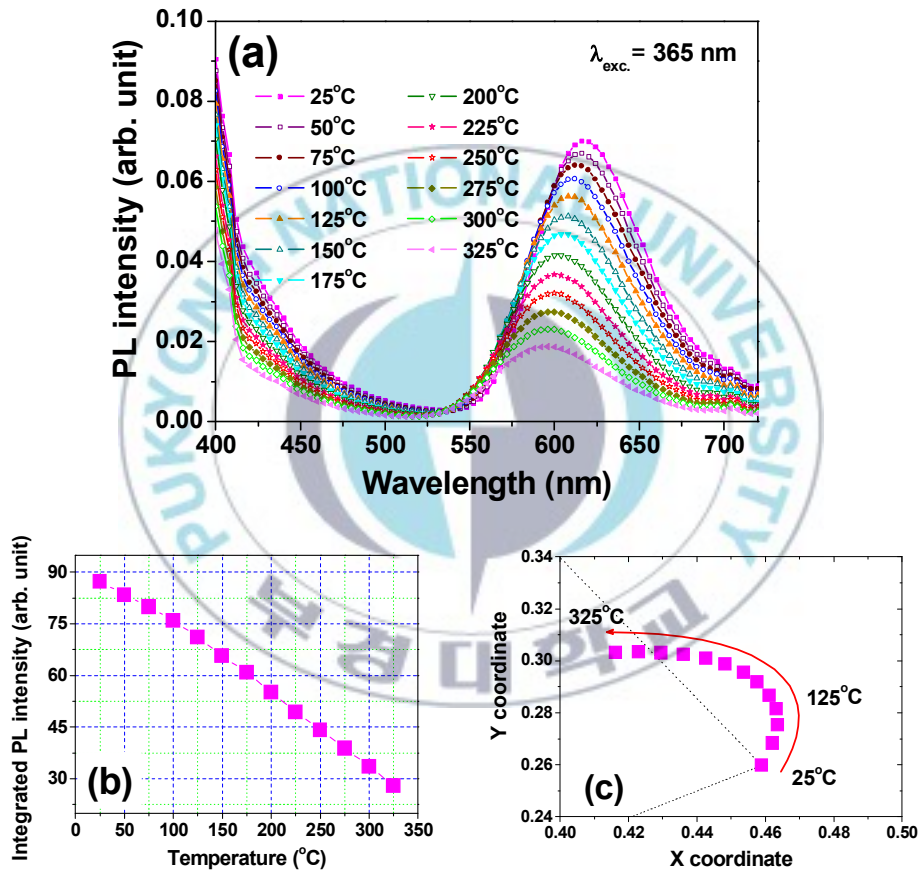


Fig. 17. Temperature-dependent PL spectra (a), integrated PL intensity (b) and color coordinates (c) from $\text{Ba}_{1.20}\text{Ca}_{0.54}\text{SiO}_4:0.10\text{Ce}^{3+}, 0.10\text{Li}^+, 0.06\text{Mn}^{2+}$ excited at 365 nm.

4.4. The mixtures of $Ba_{1.20}Ca_{0.8-2x-y}SiO_4:xCe^{3+}, xLi^+, yMn^{2+}$ and $Ba_{1.20}Ca_{0.70}SiO_4:0.10Eu^{2+}$

To enhance the low-color-rendering property due to a green-region deficiency, the blue-red $Ba_{1.20}Ca_{0.74-2x}SiO_4:xCe^{3+}/Li^+, 0.06Mn^{2+}$ phosphors are mixed with the green-emissive $Ba_{1.20}Ca_{0.70}SiO_4:0.10Eu^{2+}$ phosphor with same host lattice as the former.

Figure 18 shows the PL emission spectra (a), integrated PL intensity (b) and color coordinates (c) from $Ba_{1.20}Ca_{0.8-x}SiO_4:xEu^{2+}$ with varying Eu^{2+} concentrations. As seen in Fig. 18(a), the PL spectra exhibit a broad green emission band from 430 to 550 nm, which is characteristic of the allowed $f-d$ transition in Eu^{2+} ions. This broad spectrum is due to the spectral overlap of four different emission peaks associated with Eu^{2+} ions substituted on each of the four different Eu^{2+} sites in the T-phase $(Ba, Ca)_2SiO_4:Eu^{2+}$. The PLE spectrum from a $Ba_{1.20}Ca_{0.70}SiO_4:0.10Eu^{2+}$ phosphor monitored at 480nm and 510 nm is depicted in Fig. 18 (d). The spectrum shows a broad absorption peak which ranges from 250 nm up to 430 nm, which demonstrates that this phosphor exhibits an optimal absorption band in the near-UV (~ 400 nm) region of interest.

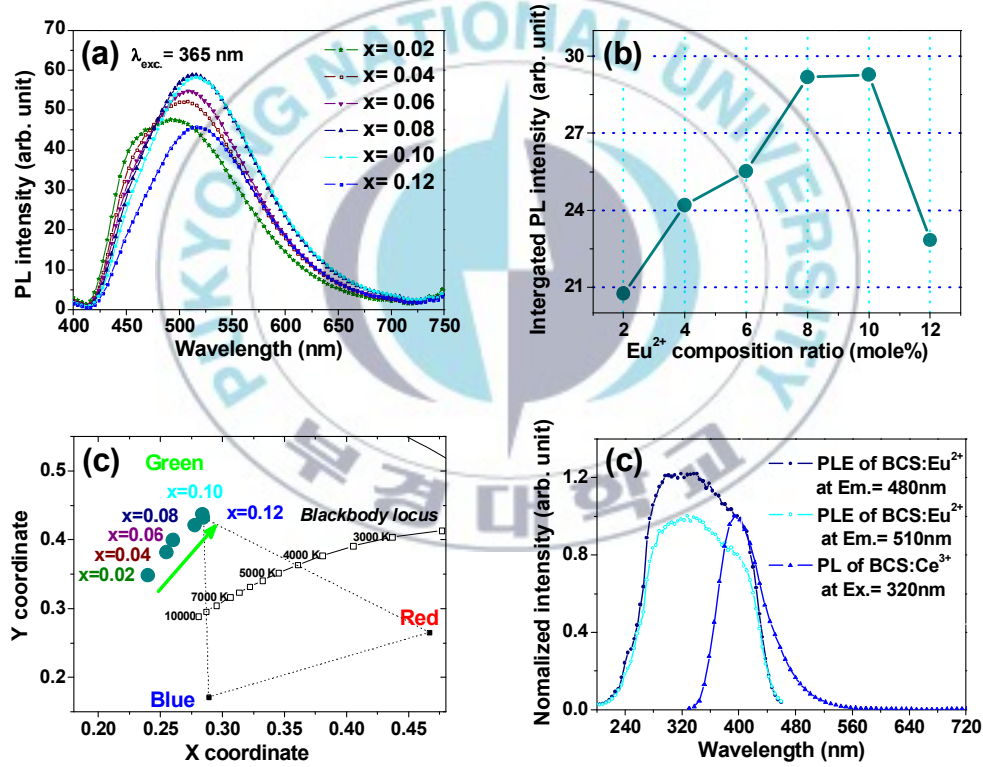


Fig. 18. PL emission spectra (a), integrated PL intensities (b) and PL emission peak color coordinates (c) from $Ba_{1.20}Ca_{0.8-x}SiO_4:xEu^{2+}$ with varying Eu^{2+} concentration ($x=0.02, 0.04, 0.06, 0.08, 0.10, 0.12$). PLE spectrum monitored at 480 and 510 nm from a $Ba_{1.20}Ca_{0.70}SiO_4:0.10Eu^{2+}$ phosphor (d).

PL spectra and color coordinates of mixture phosphors are shown in Fig. 19. As an increase of the mixture ratio of the green $\text{Ba}_{1.20}\text{Ca}_{0.70}\text{SiO}_4:0.10\text{Eu}^{2+}$ to $\text{Ba}_{1.20}\text{Ca}_{0.74-2x}\text{SiO}_4:x\text{Ce}^{3+}/\text{Li}^+, 0.06\text{Mn}^{2+}$, the color coordinates of the mixtures move to the green-color region of $\text{Ba}_{1.20}\text{Ca}_{0.70}\text{SiO}_4:0.10\text{Eu}^{2+}$. All color points of the mixtures are deviated to the red region from the straight line between both original color points. It is the reason why some deep-blue and green emissions of the mixtures are reabsorbed by the red emission. These deviations decrease for the mixtures with the more red-enhanced $\text{Ba}_{1.20}\text{Ca}_{0.74-2x}\text{SiO}_4: x\text{Ce}^{3+}/\text{Li}^+, 0.06\text{Mn}^{2+}$, i.e., the sample of higher x value. It can be considered that the reabsorption is already saturated due to the low acceptability of long-lived Mn^{2+} ions of which the ground states are easily depleted [4-12]. The mixtures show the various chromaticity of white light depending on the mixture ratio; the correlated color temperatures from 3,500 to 7,000 K, and the color rendering indices up to 95 % (see table 5).

The temperature-dependent PL spectra and PL intensities of the mixture of the green $\text{Ba}_{1.20}\text{Ca}_{0.70}\text{SiO}_4:0.10\text{Eu}^{2+}$ and $\text{Ba}_{1.20}\text{Ca}_{0.54}\text{SiO}_4:0.1\text{Ce}^{3+}/\text{Li}^+, 0.06\text{Mn}^{2+}$ excited at 365 nm are shown in Fig. 20 (a) and (b), respectively. The quenching temperature (T_q), at which the initial PL intensity is halved, is about 225 °C. This value is much higher than that of a commercial yellow $(\text{Ba}, \text{Sr})_2\text{SiO}_4:\text{Eu}^{2+}$ on a blue LED (150 °C) [4-10]. This excellent thermal stability can be explained by the configuration coordinate diagram and stokes shift [4-17].

The peak positions in the red emission spectra are blueshifted with increasing temperature: from 620 nm at 25 °C to 600 nm at 225 °C. This blueshift was commonly observed in many Eu^{2+} and Mn^{2+} doped-silicate phosphors, and explained by a phonon-assisted upconversion process called anti-Stokes shift [4-4].

The red emission in other $\text{Eu}^{2+}/\text{Mn}^{2+}$ -codoped phosphors is usually faster quenched, in contrast, for the mixture of the $\text{Ba}_{1.20}\text{Ca}_{0.70}\text{SiO}_4:0.10\text{Eu}^{2+}$ and $\text{Ba}_{1.20}\text{Ca}_{0.54}\text{SiO}_4:0.1\text{Ce}^{3+}/\text{Li}^+, 0.06\text{Mn}^{2+}$ the intensities of the green emission from Eu^{2+} decrease faster than the red emission from Mn^{2+} with increasing the temperature. It leads to the shift of the color coordinates to the red region as shown in Fig. 20 (c). This reason can be deduced from strong interaction between Ce^{3+} and Mn^{2+} in terms of energy transfer as described above.

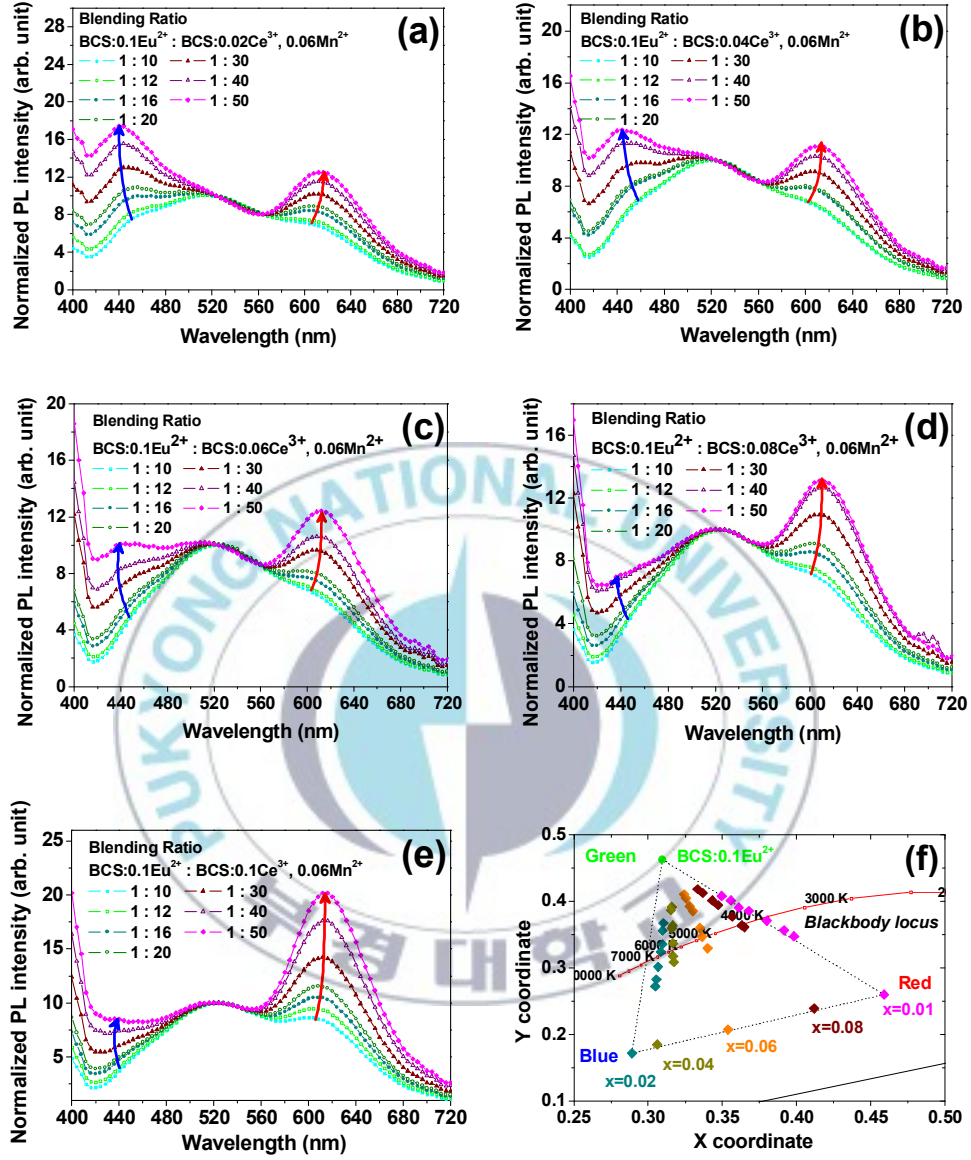


Fig. 19. Normalized emission spectra (a) ~ (e) and color coordinates (f) of the mixtures of $\text{Ba}_{1.20}\text{Ca}_{0.74-2x}\text{SiO}_4:x\text{Ce}^{3+}/\text{Li}^+, 0.06\text{Mn}^{2+}$ and $\text{Ba}_{1.20}\text{Ca}_{0.70}\text{SiO}_4:0.10\text{Eu}^{2+}$ with changing their mixture ratio.

Table 5. Color rendering indices, correlated color temperature and color coordinate of the mixtures of $\text{Ba}_{1.20}\text{Ca}_{0.74-2x}\text{SiO}_4:x\text{Ce}^{3+}/\text{Li}^+$, 0.06Mn^{2+} and $\text{Ba}_{1.20}\text{Ca}_{0.70}\text{SiO}_4:0.10\text{Eu}^{2+}$ with changing their mixture ratio.

Ce^{3+} concentration (mol%)	Mixture Ratio (wt%)	CRI	CCT (K)	Color Coordinate	
				x	y
2	1:10	85	6381	0.3102	0.3672
	1:12	89	6466	0.3097	0.3558
	1:16	95	6618	0.3096	0.3354
	1:20	97	6777	0.3086	0.3239
	1:30	91	7200	0.3067	0.3012
	1:40	83	7703	0.3055	0.2825
	1:50	79	8105	0.3048	0.272
4	1:10	79	6065	0.316	0.3916
	1:12	81	6103	0.3153	0.3868
	1:16	89	6131	0.3166	0.3634
	1:20	90	6175	0.316	0.3593
	1:30	97	6247	0.3167	0.3367
	1:40	93	6355	0.3168	0.3173
	1:50	90	6390	0.3173	0.3083
6	1:10	77	5761	0.3243	0.4102
	1:12	79	5727	0.3255	0.4042
	1:16	83	5658	0.3279	0.3922
	1:20	86	5590	0.3301	0.3849
	1:30	95	5407	0.3349	0.3598
	1:40	96	5333	0.3364	0.3466
	1:50	91	5138	0.34	0.3293
8	1:10	77	5489	0.3333	0.4181
	1:12	80	5385	0.3368	0.4123
	1:16	85	5185	0.3432	0.4012
	1:20	88	5052	0.3471	0.3942
	1:30	94	4699	0.3567	0.3769
	1:40	94	4423	0.3631	0.3635
	1:50	94	4351	0.3649	0.3611
10	1:10	85	5015	0.3496	0.408
	1:12	88	4822	0.3557	0.401
	1:16	92	4625	0.3611	0.3905
	1:20	94	4406	0.3679	0.3854
	1:30	93	3969	0.3799	0.3707
	1:40	89	3518	0.3916	0.3561
	1:50	86	3255	0.3983	0.3471

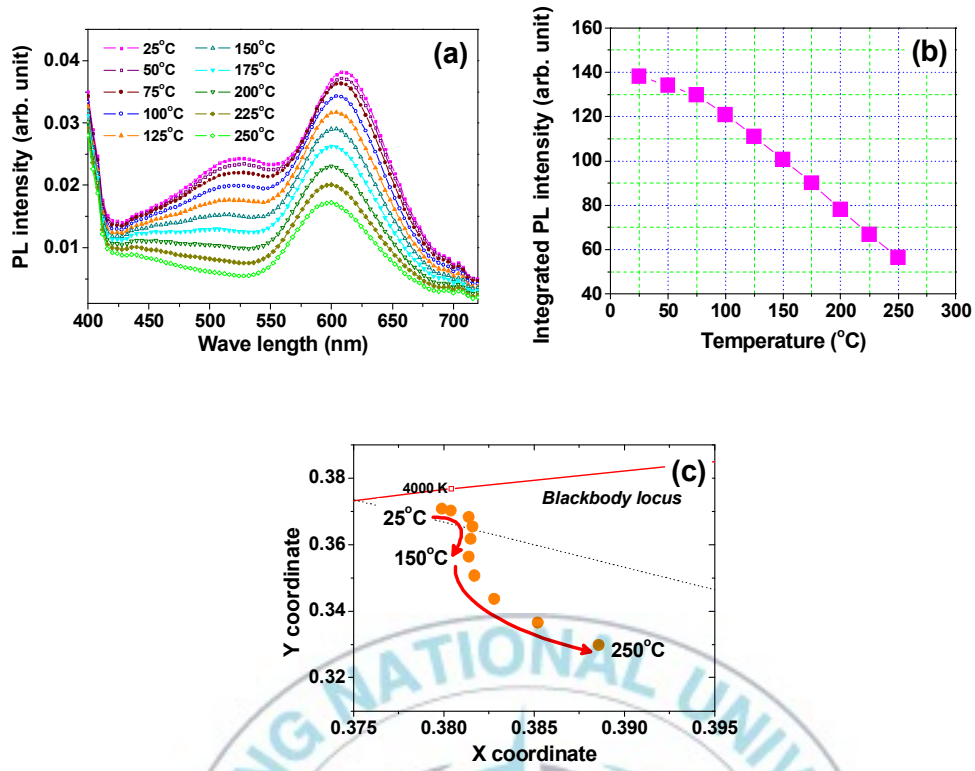


Fig. 20. Temperature-dependent PL spectra (a), integrated PL intensities (b) and color coordinates (c) of the mixtures of $\text{Ba}_{1.20}\text{Ca}_{0.54}\text{SiO}_4:0.1\text{Ce}^{3+}/\text{Li}^+$, 0.06Mn^{2+} and $\text{Ba}_{1.20}\text{Ca}_{0.70}\text{SiO}_4:0.10\text{Eu}^{2+}$.

5. CONCLUSIONS

T-phase phosphors were obtained in binary $\text{Ba}_2\text{SiO}_4\text{-Ca}_2\text{SiO}_4$ systems activated by trivalent cerium, divalent europium and divalent manganese through a conventional solid-state reaction technique. Phosphors in the region of $\text{Ba}_{1.2}\text{Ca}_{0.8}\text{SiO}_4\text{-Ba}_{0.8}\text{Ca}_{1.2}\text{SiO}_4$ are identified as T phase under the space group $P\bar{3}m1$ with hexagonal unit cell whereas the others are identified as α , β , γ phase in the order of increasing Ca compositions. Only T phase in the binary $\text{Ba}_2\text{SiO}_4\text{-Ca}_2\text{SiO}_4$ systems has a single octahedral Ba/Ca site with 6-coordination number, whereas other systems including pure Ba_2SiO_4 and Ca_2SiO_4 compounds have two different Ba/Ca/ polyhedrons with more than 9-coordination number. The efficient red emission from Mn^{2+} ions is possible only for T-phase $(\text{Ba}, \text{Ca})_2\text{SiO}_4$ host lattice, and they show the most thermally stable optical-properties. For single Mn^{2+} -doped T-phase phosphor, red emissions from Mn^{2+} ions are not observed. However, a distortion of Mn^{2+} site symmetry and the violation of Mn^{2+} selection rule are induced by codoping Ce^{3+} ions. Consequently the orders-of-magnitude enhancement of the red emission from Mn^{2+} ions appears suddenly as well as the deep-blue emission bands from Ce^{3+} ions.

Therefore, to achieve efficient red emission bands from Mn^{2+} it is necessary to have follow requirements; (i) it is desirable for the structure of host lattice to have octahedral or tetrahedral cation sites (i.e., 4 or 6 coordinate cation sites), (ii) some environments should be required to enable optically forbidden transition to be allowed such as local distortion, strong crystal field, strong LS coupling. Namely energy transfer between Mn^{2+} ion (acceptor) and the others (donor) should be possible to lift rigid selection rules.

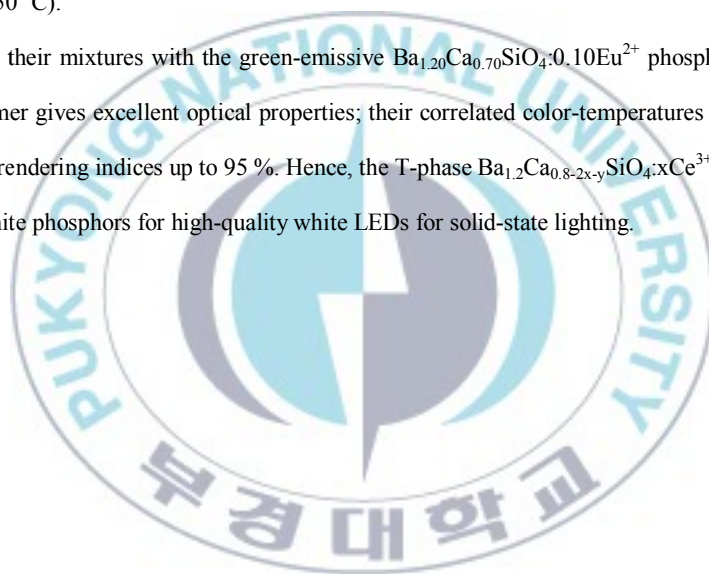
The following phosphors have developed for high-quality white-light generation.

(i) A novel deep-blue phosphor, T-phase $\text{Ba}_{1.2}\text{Ca}_{0.8}\text{SiO}_4\text{:Ce}^{3+}$, has been developed for white-light-emitting diodes. The expansion of the host lattice by doping Ce/Li ions demonstrates they prefer to occupy Ca sites rather than Ba sites all over five different Ca/Ba sites. The phosphor exhibits two absorption bands at 280 nm and 325 nm due to the characteristic doublet of Ce^{3+} ions, and an intense deep-blue emission peaking at 400 nm. The strong correlate on between the lattice constants and the emission peaks is explained by the crystal field effect and the configurational coordinate diagram; with increasing Ce/Li ions, the lattice constants increase along with the emission peaks blueshifting. It shows much higher thermal quenching

temperature (225 °C) due to a weak electron-phonon interaction. Thus, the $\text{Ba}_{1.2}\text{Ca}_{0.8}\text{SiO}_4:\text{Ce}^{3+}$ phosphor can be used as a sensitizer phosphor to excite other green or red phosphors as well as a promising blue phosphor for white LED for solid state lighting.

(ii) The T-phase $\text{Ba}_{1.20}\text{Ca}_{0.8-2x-y}\text{SiO}_4:x\text{Ce}^{3+}/\text{Li}^+, y\text{Mn}^{2+}$ phosphors show the deep-blue at 400 nm from Ce^{3+} ions and the red from Mn^{2+} ions. According to crystal field theory, the lattices expand along with increasing Ce^{3+} ions, leading to the strong blue shift in the blue band, while they shrink along with increasing Mn^{2+} ions, causing to the strong red shift in the red band. As an increase of Ce^{3+} concentrations at a fixed Mn^{2+} concentration, the EPR line widths are broadening and shifting to the higher-field side. It implies that the doped Ce^{3+} ions make a distortion of Mn^{2+} site symmetry, which is consistent with shortening of Mn^{2+} acceptor decay times so as to enhance Mn^{2+} intensity. The phosphor show a higher quenching temperature of about 250 °C for both emission bands/colors than that of a commercially used yellow-emitting $(\text{Ba}, \text{Sr})_2\text{SiO}_4:\text{Eu}^{2+}$ (150 °C).

(iii) Finally, their mixtures with the green-emissive $\text{Ba}_{1.20}\text{Ca}_{0.70}\text{SiO}_4:0.10\text{Eu}^{2+}$ phosphor with same host lattice as the former gives excellent optical properties; their correlated color-temperatures from 3500 to 7000 K, and the color-rendering indices up to 95 %. Hence, the T-phase $\text{Ba}_{1.2}\text{Ca}_{0.8-2x-y}\text{SiO}_4:x\text{Ce}^{3+}, y\text{Mn}^{2+}$ phosphors are promising white phosphors for high-quality white LEDs for solid-state lighting.



REFERENCES

- [1-1] Schubert, E.F. “*Light Emitting Diodes*” (Cambridge, Cambridge University Press, 2003).
- [1-2] Bando, K., Sakano, K., Noguti, Y., and Shimizu, Y., *Tech. Digest, Phosphor Res. Soc.*, 264th Meeting, 5, (in Japanese, 1996).
- [1-3] Bando, K., Sakano, K., Noguti, Y., and Shimizu, Y., *J. Light Vis. Environ.* **22** (1998) No.1, 2–5.
- [1-4] L. S. Rohwer and A. M. Srivastava, *Electrochem. Soc. Interface* **12**(2) (2003) 36.
- [1-5] M. G. Craford, *Commercial, Light Emitting Diode Technology*, Kluwer Academic Publishers, Dordrecht, 1996.
- [1-6] J. S. Kim, P. E. Jeon, J. C. Choi, S. I. Mho, G. C. Kim, and H. L. Park, *Appl. Phys. Lett.*, **84** (2004) 2931.
- [1-7] A. A. Setlur, J. J. Shiang, and U. Happek, *Appl. Phys. Lett.* **92**, 081104 (2008).
- [1-8] J. S. Kim, P. E. Jeon, J. C. Choi, S. I. Mho, G. C. Kim, H. L. Park, *Appl. Phys. Lett.* **84** (2004) 2931.
- [1-9] S. Ye, J. Zhang, X. Zhang, S. Lu, X. Ren, X. Wang, *J. Appl. Phys.* **101** (2007) 033513.
- [1-10] W. J. Yang, L. Luo, T. M. Chen, N. S. Wang, *Chem. Mater.* **17** (2005) 3883.
- [1-11] B. Matković, S. Popović, B. Gržeta, *J. Am. Ceramic. Soc.* **69**, 132 (1986).
- [1-12] B. K. Okada, and J. Ossaka, *Acta Crystallogr.* **B36** (1980) 919.
- [2-1] Nakamura, S., Mukai, T., and Senoh, M., *Appl. Phys. Lett.*, **64** (1994) 1687–1689.
- [2-2] Muller-Mach, R., Muller, G.O., Krames, M.R., and Trottier, T., *IEEE J. Sel. Top. Quantum Electron.*, **8**, No.2 (2002) 339–345.
- [2-3] Taguti, T., *J. Light Vis. Environ.*, **27**, No.3 (2003) 131–139.
- [2-4] Starrick, D., et al., *Proceedings of Phosphor Global Summit*, (2003).
- [2-5] J. K. Park, M. A. Lim, C. H. Kim, H. D. Park, J. T. Park, *Appl. Phys. Lett.*, **82** (2003) 683.
- [2-6] Xie, R.J., Mitomo, M., Uheda, K., Xu, F.F., and Akimune., *J. Am. Ceram. Soc.*, **85** (2002) 1229.
- [2-7] van Krevel, J. W. H., van Rutten, J. W. T., Mandal, H., Hintzen, H. T., and Metselaar, R., *J. Solid State Chem.* **165** (2002) 19.
- [2-8] Li, Y. Q., Delsing, A. C. A., de With, G., and Hintzen, H. T., *Chem. Mater.* **17** (2005) 3242–3248.
- [2-9] Yamada, M., Naitou, T., Izuno, K., Tamaki, H., Murasaki, Y., Kameshima, M., and Mukai, T., *Jpn. J. Appl. Phys.*, **42**, No.2 (2003) L20.

- [2-10] Blasse, G., Wanmaker, W.L., Tervrugt, J.W., and Bril, A., *Philips Res. Rept.*, **23** (1968) 189.
- [2-11] Di Bartolo B, “*Optical interactions in solids*” (Wiley, New York, 1968).
- [2-12] Blasse, G., Material science of the luminescence of inorganic solids, in “*Luminescence of Inorganic Solids*” (DiBartolo, B., Ed., Plenum Press, 1978, 457).
- [2-13] Urbach, F., Pearlman, D., and Hemmendinger, H., *J. Opt. Soc. Am.*, **36** (1946) 372.
- [4-1] B. K. Okada, and J. Ossaka, *Acta Crystallogr.* **B36** (1980) 919.
- [4-2] K. Fukuda, M. Ito, and T. Iwata, *J. Solid State Chem.* **180** (2007) 2305.
- [4-3] B. Matković, S. Popović, B. Gržeta, *J. Am. Ceramic. Soc.* **69** (1986) 132.
- [4-4] J. S. Kim, P. E. Jeon, J. C. Choi, S. I. Mho, G. C. Kim, H. L. Park, *Appl. Phys. Lett.* **84** (2004) 2931.
- [4-5] S. Ye, J. Zhang, X. Zhang, S. Lu, X. Ren, X. Wang, *J. Appl. Phys.* **101** (2007) 033513.
- [4-6] W. J. Yang, L. Luo, T. M. Chen, N. S. Wang, *Chem. Mater.* **17** (2005) 3883.
- [4-7] G. Blasse, and B.C. Grabmaier, “*Luminescent Materials*” (Springer, Berlin Heidelberg, 1994).
- [4-8] G. Blasse, *Philips Res. Rept.*, **24** (1969) 131.
- [4-9] P. Dorenbos, *J. Lumin.*, **104** (2003) 239.
- [4-10] J. S. Kim, Y. H. Park, J. C. Choi, and H. L. Park, *J. Electrochem. Soc.*, **152** (2005) H135.
- [4-11] Z. Hao, Z. Nie, S. Ye, R. Zhong, X. Zhang, L. Chen, X. Ren, S. Lu, X. J. Wang, and J. Zhang, *J. Electrochem. Soc.* **155** (2008) H606.
- [4-12] A. A. Setlur, J. J. Shiang, and U. Happek, *Appl. Phys. Lett.* **92** (2008) 081104.
- [4-13] B. Henderson, and G. F. Imbusch, “*Optical Spectroscopy of Inorganic Solids*” (Clarendon press, Oxford, 1989).
- [4-14] J. Gorn, G. Opbroek, K. Post, and H. W. Hartog, *Phys. Rev.* **B 30** (1984) 3608.
- [4-15] B. P. Maliwal, Z. Gryczynski, and J. R. Lakowicz, *Anal. Chem.* **73** (2001) 4277.
- [4-16] J. S. Kim, Y. H. Park, J. C. Choi, and H. L. Park, *J. Electrochem. Soc.*, **152** (2005) H135.
- [4-17] S. Shionoya and W.M. Yen, “*Phosphor Handbook*” (CRC Press, NY, 1998).

국문요약

$\text{Ba}_2\text{SiO}_4\text{-Ca}_2\text{SiO}_4$ 이성분계내 백색 발광 소자용 T-phase 형광체 특성 연구

$\text{Ba}_2\text{SiO}_4\text{-Ca}_2\text{SiO}_4$ 이성분계 내 모체에 Ce^{3+} , Eu^{2+} , Mn^{2+} 이온이 도핑된 형광체를 환원 분위기상의 고상 반응을 통해 각각 제작하고 백색 발광소자용 형광체로 이용하기 위해 발광특성을 연구하였다. 먼저 청색 발광 형광체로써 $\text{Ba}_{1.2}\text{Ca}_{0.8-2x}\text{SiO}_4:\text{xCe}^{3+}/\text{Li}^+$ 와 청색과 적색을 동시에 발광하는 $\text{Ba}_{1.2}\text{Ca}_{0.8-2x-y}\text{SiO}_4:\text{xCe}^{3+}, \text{yMn}^{2+}$ 형광체를 합성하고, 상기 합성된 $\text{Ba}_{1.2}\text{Ca}_{0.8-2x-y}\text{SiO}_4:\text{xCe}^{3+}, \text{yMn}^{2+}$ 형광체와 녹색발광 $\text{Ba}_{1.2}\text{Ca}_{0.7}\text{SiO}_4:0.1\text{Eu}^{2+}$ 형광체의 혼합을 통해 백색광을 구현하였다. X 선 회절 패턴 분석을 통해 $\text{Ba}_2\text{SiO}_4\text{-Ca}_2\text{SiO}_4$ 이성분계 내에서 $\text{Ba}_{1.2}\text{Ca}_{0.8}\text{SiO}_4\text{-Ba}_{0.8}\text{Ca}_{1.2}\text{SiO}_4$ 의 조성비 범위 내의 형광체는 $P3m1$ 의 공간구조군을 가지는 육방정계구조의 T-phase임을 확인하였다. 상기 조성비 내 T-phase 구조를 가지는 형광체는 $\text{Ba}_2\text{SiO}_4\text{-Ca}_2\text{SiO}_4$ 이성분계 내에서 유일하게 6 배위수의 양이온 자리가 존재함으로써 그 자리에 치환된 Mn^{2+} 이온이 광학적으로 활성화되어 높은 효율의 적색발광이 가능함을 확인하였다.

$\text{Ba}_{1.2}\text{Ca}_{0.8-2x}\text{SiO}_4:\text{xCe}^{3+}/\text{Li}^+$ 형광체는 280 nm 와 325 nm 에서 최대 흡수 특성을 보이며, 400 nm 부근에서 강한 청색 발광이 나타남을 확인하였다. 또한, 이 T-phase 형광체는 225°C의 높은 온도소광 특성을 나타낸다. Ce/Li 이온의 도핑에 따른 모체 격자의 팽창은 Ce/Li 이온이 Ba 자리 보다 Ca 자리에 우선적으로 치환됨을 입증하며, 결정장 효과에 의한 발광 파장의 변화는 격자 상수의 변화와 연관됨을 확인하였다.

Ce^{3+} 과 Mn^{2+} 이온이 이중으로 도핑된 T-상의 $(\text{Ba}, \text{Ca})_2\text{SiO}_4$ 형광체는 600 nm 부근의 적색발광과 400 nm 부근의 청색발광을 동시에 보이며, 이는 Mn^{2+} 의 ${}^4\text{T}_1\text{-}{}^6\text{A}_1$ 금지된 전이와 Ce^{3+} 의 4f-5d 허용된 전이 특성에 기인한다. 상기 T-phase 의 $(\text{Ba}, \text{Ca})_2\text{SiO}_4$ 동일모체에 Mn^{2+} 이온만을 단독으로 도핑 하였을 경우 적색발광을 관측할 수 없었으며, 미량의 Ce^{3+} 이온을 Mn^{2+} 이온과 함께 도핑 하였을 때 청색 및 적색 발광이 동시에 나타남을 확인하였다. 본 연구를 통해 Ce^{3+} 와 Mn^{2+} 이온간의 강한 상호작용을

에너지 전이 이론과 결정장 효과 및 도핑에 따른 결정구조의 미세변화의 관점에서 조사하였다. 발광 천이시간 측정 결과와 전자 상자성 공명 측정결과와의 상호관계는 Ce^{3+} 이온의 도핑에 따라 Mn^{2+} 이온자리 주변의 국지적 결함을 야기시킴으로써 선택규칙에 반하는 광 활성 전이가 가능케 됨을 설명해준다. 또한 상기 형광체는 발광 소자의 구동 온도 (125°C) 보다 높은 온도소광 온도 (250°C)의 특성을 나타낸다.

마지막으로 상기 합성된 형광체를 자외선 발광 소자를 근간으로 한 백색발광 소자에 적용하기 위해 청색 및 적색을 발광하는 $\text{Ba}_{1.2}\text{Ca}_{0.8-2x-y}\text{SiO}_4:\text{xCe}^{3+}, \text{yMn}^{2+}$ 형광체와 넓은 영역의 녹색을 발광하는 동일구조의 $(\text{Ba,Ca})_2\text{SiO}_4:\text{Eu}^{2+}$ 형광체를 혼합하여 백색광을 구현하였으며, 상기 혼합 형광체는 혼합 비율에 따라 상관 색온도가 3500 K 부터 7000 K 에 이르는 다양한 발광색 재현이 가능하며 95 의 고연색지수 값을 나타냄을 확인하였다.

따라서, 본 연구를 통한 $\text{Ba}_{1.2}\text{Ca}_{0.8-2x-y}\text{SiO}_4:\text{xCe}^{3+}, \text{yMn}^{2+}$ 형광체와 이를 이용한 백색발광소자는 종래 디스플레이 백색광원 뿐만 아니라 고연색 및 장시간 구동에 있어 안정적인 백색광을 필요로 하는 실내 조명용 백색발광소자까지 응용이 가능 하다.



핵심 되는 말: $\text{Ba}_{1.2}\text{Ca}_{0.8}\text{SiO}_4$ 형광체, 결정장 효과, 에너지 전이, 온도 소광, 백색 발광소자